Atomic-Scale Simulations of Solvent Decomposition and Solid-State Ion Transport in Alkaline-based Batteries

by

Mallory R. Fuhst

A dissertation submitted in partial fulfillment
of the requirements for the degree of
Doctor of Philosophy
(Applied Physics)
in the University of Michigan
2024

Doctoral Committee:

        Professor Çagliyan Kurdak, Co-Chair
        Professor Donald J. Siegel, University of Texas at Austin, Co-Chair
        Professor Udo Becker
        Professor Wei Lu
        Associate Professor Liang Qi

Mallory R. Fuhst

fuhstma@umich.edu

ORCID iD: 0000-0002-1086-0317

Dedication

To Luis and Orion.

Acknowledgements

I'd like to thank my advisor, Dr. Don Siegel, and my groupmates in the Energy Storage and Materials Simulation Lab. Thank you for countless interesting discussions and unquantifiable help. Thanks also go out to the Applied Physics Program, in particular Dr. Çagliyan Kurdak, Cyndi McNabb, and Lauren Segall. Thank you for always providing a supportive and welcoming home base during graduate school (and also for all the pizza).

To my family, both biological and found, I couldn't have done this without your continuous, unflinching support and unwavering belief in me. This is your win as much as mine – there is no way this would have happened without you.

Finally, I'd like to thank myself. You stuck through so much. Thank you for having the courage to step away and reevaluate, and then return and stick through it yet again.

Table of Contents

List of Tables

List of Figures

Abstract

Improving the safety of rechargeable Li-ion batteries is needed given their widespread and growing use. Of particular concern are failures involving thermal runaway, a key contributor of which is the buildup of gaseous species in the cell. Gases develop from the degradation of the liquid electrolyte, potentially facilitated by interactions with the electrode surfaces. The first portion of this dissertation investigates these processes by using first principles calculations to model the interactions of a common electrolyte solvent molecule with a cathode surface. These materials are thought to be electrochemically stable, but renormalization of the electrolyte window at the cathode surface may lead to side reactions even within normal battery operating conditions. Our work finds that the undercoordinated Co ions on the $(10\bar{1}4)$ low energy surface of $LiCoO_2$ are in an intermediate spin state that makes them more receptive to electrostatic coordination with EC. The barrier for the decomposition of EC into CO_2 and acetaldehyde is 2.1 eV, which suggests a kinetically limited reaction pathway at nominal operating temperature. This barrier is expected to decrease as the cathode is delithiated during charging.

Another strategy for increasing the safety of rechargeable batteries is to switch to a solid-state electrolyte (SSE). SSEs are more stable, but struggle to match a liquid's high ionic conductivity. One avenue for increasing the conductivity of an SSE is the paddlewheel effect: coordinated motion between a rotating anion group and a migrating cation. First reported for the high temperature (HT) polymorph of Li_2SO_4, the existence of this phenomena has been the subject of debate for decades. The second component of this dissertation uses aiMD to model

dynamics associated with Li migration in high- and low-temperature (LT) Li_2SO_4. Analysis of the rotational dynamics of the anions reveals that the SO_4 anions reorient in the HT polymorph but not the LT polymorph, even at temperatures above the phase transition. Likewise, the simulations identify numerous Li migration events in the HT phase but none in the LT polymorph. These observations are consistent with experimental measurements. Analysis of Li displacements and anion rotations in the HT phase indicate that cation hops and anion reorientations are correlated in space and in time. Additional evidence supporting correlated behavior derives from the similar the energy barrier for Li migration, 0.48 eV, and anion reorientation, 0.40 eV.

To further probe the mechanisms associated with paddlewheel dynamics, the third portion of this dissertation draws comparisons with other alkali-metal-based sulfates, Na_2SO_4 and K_2SO_4. These solids exhibit structural transformations similar to that of Li_2SO_4, yet are not reported to be ionic conductors in their HT phases. Consistent with experiments, aiMD simulations exhibit limited cation mobility in these phases. Nevertheless, anion rotations are present in both HT Na_2SO_4 and K_2SO_4. Given that anion rotations are present in all of the HT polymorphs studied, why is Li_2SO_4 the only phase that is ionically-conductive? The crystal structure of the HT polymorphs appears to be the answer. HT-Li_2SO_4 adopts an FCC lattice that contains occupied Li tetrahedral sites and vacant octahedral sites, which mediate Li migration. HT Na_2SO_4 and K_2SO_4 are hexagonal and contain no empty cation sites. We conclude that the presence of anion rotations alone is insufficient to impart high ionic conductivity – cation mobility also requires a sufficient defect concentration.

Chapter 1 Introduction

1.1 Electrochemical energy storage

As energy demands increase, we find ourselves in need of novel ways to produce, store, and distribute electricity. Combating climate change requires us to find alternatives to our dependence on fossil fuels, but the chemical potential stored in coal and gasoline is difficult to replicate in terms of stability and portability. Likewise, mistakes in transporting oil can cause environmental disasters, but it's difficult to find an easier, faster, and cheaper way to fuel vehicles. While solar and wind energy are renewable, their intermittency present challenges compared to the consistency of fossil fuels. We need a way to store electrical energy both on the grid and portably that has the low costs and high energy density of fossil fuels, but without the harmful carbon associated with the combustion of hydrocarbons. Batteries present arguably the most promising mechanism for storing electrical energy, but must continue to improve to address the everchanging energy landscape.

Li-ion batteries (LIBs) comprise the majority of portable rechargeable batteries at present.[1,2] The three basic components of an LIB are the anode, cathode, and electrolyte. In a conventional LIB, the anode is graphite, the cathode is a transition metal oxide, and

Figure 1.1 Electronic structure of Li-ion battery with renormalized HOMO/LUMO levels. Adapted with permission from Ref 3 © 2016 American Chemical Society.

the liquid electrolyte is a mixture of a lithium salt and organic solvents. The theoretical voltage of a battery is determined by the difference in the electrochemical potential (fermi energy) between the anode and cathode. Practically, the voltage is constrained by the electrochemical stability of the electrolyte.[1,3] As shown in Figure 1.1, if the lowest unoccupied molecular orbital (LUMO) of the electrolyte is below the electrochemical potential of the anode (μ_A), or the highest occupied molecular orbital (HOMO) is above the electrochemical potential of the cathode (μ_C), the electrolyte is unstable, as this would allow electrons to travel from the anode into the electrolyte or from the electrolyte to the cathode, either of which has the potential to decompose the electrolyte.[3] The electrolyte must be an electronic insulator to avoid being reduced/oxidized at the anode/cathode surface, as well as being a good ionic conductor that readily shuttles Li^+ ions between the terminals.

Ideally, the LUMO of the electrolyte will be above the electrochemical potential of the anode and the HOMO will be below the electrochemical potential of the cathode, with the gap between the LUMO and HOMO defined as the electrolyte's stability window. Based on these stability criteria, it is surprising to note that the fermi level of graphite, the commonly-used anode in today's LIB's, is well above the LUMO of most LIB electrolytes, potentially resulting in the undesirable reduction of the electrolyte at the anode surface.[4,5] However, with a suitable choice for the composition of the electrolyte, this interfacial reaction process can result in the formation of the so-called solid electrolyte interphase (SEI). An ideal SEI will passivate the anode surface, preventing further reaction with the electrolyte, while allowing Li-ion transport and hindering electronic conductivity.[1,2,6] At the positive electrode, oxidation of the electrolyte by the cathode active material is in theory less likely (μ_C > HOMO) for materials used in common LIBs.[2] However, interactions between the solvents/salts/electrodes can lead to the

2

renormalization of the HOMO levels.[3] If the HOMO energy is lowered, the cathode may be able to oxidize the electrolyte and lead to the formation of a CEI – a cathode-electrolyte interphase. The CEI is less well-studied compared to the SEI, presumably because it is not as ubiquitous as the SEI, and its properties appear to have less of an impact on cell performance.[1]

1.2 Electrolyte gassing in lithium ion batteries

In addition to the formation of solid phases at the interface between the electrodes and electrolyte, these interfacial reactions can also generate gaseous species inside the sealed cell.[7–10] As shown in Figure1.2a, as the temperature increases, gases begin to develop in the cell. These exothermic reactions add more energy to the system, driving the temperature higher and spurring the creation of more gases, eventually catapulting the system into thermal runaway.[11,12] This process is commonly caused by overheating, overcharging, or mechanical abuse, leading to either the thermal decomposition of the electrolyte or its reduction/oxidation at the anode or cathode surfaces. Upon examination of the vapors released during thermal runaway in a LIB, CO_2 has been identified a major component, as was H_2 and ethylene for a standard ethylene
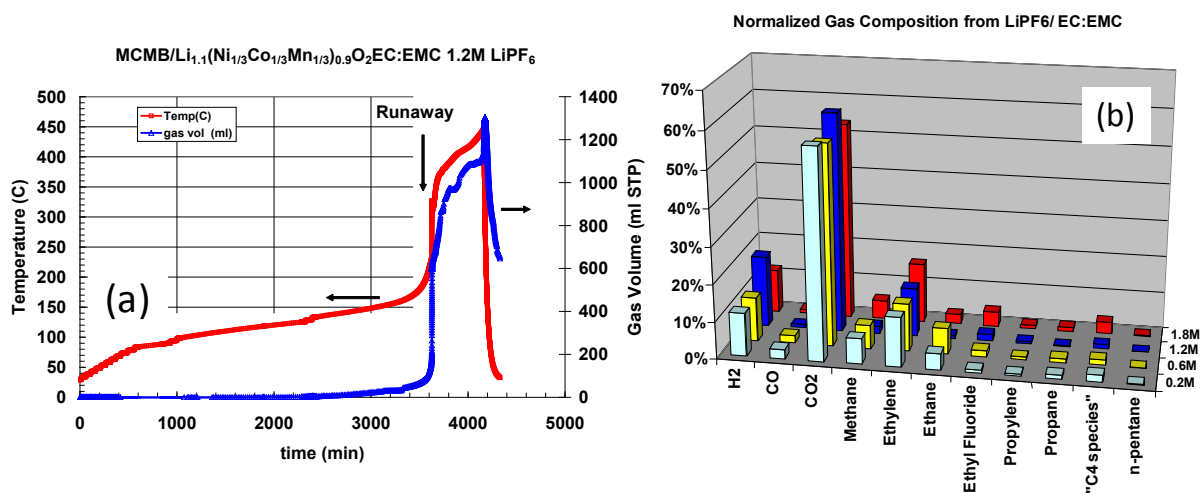
Figure 1.2 Experimental results on gas generation during thermal runaway in a lithium ion battery. Adapted from Ref 11.

3

carbonate (EC) based electrolyte, as shown in Figure 1.2b. While CO_2 is non-flammable,

pressure build-up in cell can result in venting of the volatile solvent vapors, which in turn present

a safety hazard. Furthermore, the same study found that the amount of salt in the electrolyte

played a role in determining when gases would begin to accumulate in the cell, showing that the

electrolyte composition impacts the electrolyte decomposition reaction dynamics.[11]

The 3rd chapter of this dissertation explores the decomposition of EC on the surface of

$LiCoO_2$ (LCO), a common cathode material. Experiments suggest that EC can thermally

decompose into CO_2 and acetaldehyde, both of which have been observed in LIB thermal

runaway.[11,12] The impact of the cathode surface on the energetics and mechanism of the EC

decomposition reaction are not well-understood. The atomic-scale insights provided by this study

will be helpful in the design of a safer Li-ion battery.

1.3 Paddlewheel mechanism of ionic conduction in solid-state electrolytes

Safety concerns associated with the use of LIBs are not theoretical: examples include

travel restrictions of li-ion batteries to electric car fires to exploding phones. One option for

improving the safety of battery systems is doing away with the liquid electrolyte altogether and

moving to a solid-state battery (SSB). Advantages of solid electrolytes (SE) are that they are

incombustible, nonvolatile, nonflammable, stable at elevated temperatures, can have a wide

stability window, and won't leak.[13]

However, SEs come with their own set of challenges. The primary limitation in the

development of solid state batteries is the lower ionic conductivity of the SE compared to that of

liquid electrolytes. Additional challenges include microstructural influences on conductivity

(e.g., at grain boundaries), wettability and reactivity at the interfaces between SE and electrodes,

manufacturing challenges, internal resistance, and low current density compared to liquid

electrolytes.[13] Future developments of SE must therefore overcome these challenges to able to compete with the typical 10^{-2}-10^{-1} S cm^{-1} conductivities of liquid electorlytes.[13]

The second and third portions of this dissertation investigate prototype solid electrolytes. A promising group of emerging SE materials takes advantage of a conduction mechanism known as the paddlewheel effect. The paddlewheel effect exists when there is a correlation in space and time between the migration of a cation and anion reorientations. The migration and reorientation should have similar energetics and a similarity in translation vibration/libration modes. It is important to note that this term does not imply causation between the anion rotations and cation motion. In this dissertation, the paddlewheel effect is a recognition of the correlation.

This term was first coined following studies of the behavior of the high temperature phase of Li$_2$SO$_4$ (LSO). The dramatic increase in ionic conductivity in LSO upon transformation into the high

Figure 1.3 Conductivity of Li$_2$SO$_4$ and Na$_2$SO$_4$ through their respective solid-solid phase changes. Adapted from Ref 85.

temperature alpha phase was first noted in 1921.[14] At temperatures above 850 K, LSO transforms from a monoclinic to a face-centered cubic structure, and the ionic conductivity jumps from 10^{-7} S cm^{-1} at 470 K to 1.07 S cm^{-1} at 860 K.[15,16] Remarkably, the conductivity of the high-temperature polymorph is comparable to that of the liquid (molten) state.

5

In the 1950's, x-ray diffraction on the alpha phase suggested that the orientations of the tetrahedral SO_4^{2-} anions are disordered, and potentially free to rotate.[17] In light of these two observations, in 1973 Kvist and Bengtzelius proposed that the anomalous increase in ionic conductivity of the HT phase was due to coordinated movements of the migrating Li^+ ions and the rotating sulfates.[18] This transport model became variously known as the 'cog-wheel,' 'revolving door,' or 'paddlewheel' mechanisms, and has been the source of much debate regarding whether anion rotations exist, and, if they do, the degree of their impact upon the mobility of the cations.

Proving the existence and importance of the paddlewheel mechanism on ionic conductivity has proved to be challenging. In the decades following its conception, numerous articles were published defending the existence of the paddlewheel mechanism in LSO and other materials that exhibit high temperature rotor phases.[15,17,19–24] However, others argued that the paddlewheel mechanism was an artifact of the lattice expansion that typically accompanies a polymorphic structural transition to the high temperature phase. These authors argued that the increase in volume was the differentiating factor, and that increase in ionic conductivity resulted from an enhanced percolation mechanism.[25–28] Despite decades of investigation, the atomic-scale dynamics that underlie these processes have proven difficult to discern experimentally,[29] due to the pico-second timescale of the associated rotational and translational events, and difficulties in differentiating between static and dynamic disorder of the anions. Furthermore, the few computational studies conducted on LSO were classical in nature and did not fully characterize the potential correlations between anion rotations and cation translational dynamics.[20,30–32]

The second portion of this dissertation reexamines the paddlewheel effect in LSO, testing an aiMD model of the low and high temperature phase for cooperative motion between anion

rotations and cation migrations. Characterizing the ionic conduction mechanisms in this benchmark system will help further identify potential fast-ion conductors and their underlying conduction mechanisms.

The third portion of this dissertation examines Na_2SO_4 (NSO) and K_2SO_4 (KSO) for anion reorientations and cation migration mechanisms. Chemically similar to LSO, NSO and KSO also have an orientationally disordered high temperature phase but are not fast-ion conductions. There is considerable debate in the literature on the nature of the disorder in the sulfate tetrahedra. The simulations here will attempt to ascertain if the disorder is static or dynamic, and discern how that impacts cation migration events. We hope to identify the difference that allows LSO to be a fast ion conductor while the other alkaline sulfates are not. In doing so, we may aid in the prediction of other materials that benefit from the paddlewheel effect and the development of new solid-electrolytes.

1.4 Goals of this dissertation

Chapter 3 aims to model the surface of LCO and ascertain the magnetic ordering of surface Co ions. From there, classical and first principles will be employed to determine non-dissociative adsorption of a molecule of EC on the surface. The molecule will be decomposed to discover potential reaction products and configurations, and the thermodynamics driving force of the decomposition. Finally, transition state theory will be used on the most exothermic of the reactions to estimate the energy barriers and therefore the reaction rate.

In Chapter 4 this work will transition to solid electrolyte materials. Ab initio molecular dynamics calculations will be employed to simulate the migration in high and low temperature polymorphs of LSO. The correlation between anion reorientations and cation displacement will be studied to determine the role of the paddlewheel effect in this material.

Finally, Chapter 5 will probe the high and low temperature polymorphs of NSO and KSO for anion disorder and cation migrations. The aiMD studies will seek to discern if the experimentally verified orientational disorder in the sulfate tetrahedra is static or dynamic in the high temperature phases of these materials. The cation migration will also be studied, and an attempt made to answer the question of why chemically similar LSO is a fast-ion conductor while NSO and KSO are not.

There is still so much we don't understand about electrochemistry, even the benchmark systems considered in this dissertation that have been the subjects of decades of study. First principles simulations may be able to fill in these gaps, expanding our understanding of theory and enhancing our ability to predict experimental results.

.

Chapter 2 Methodology

2.1 Density Functional Theory

The Schrodinger equation is used to predict system behavior in the quantum realm. The non-relativistic and time-independent Schrodinger equation can be written as

$$\left[-\frac{\hbar^2}{2m} \sum_{i=1}^{N} \nabla_i^2 + \sum_{i=1}^{N} V(r_i) + \sum_{i=1}^{N} \sum_{j<i} U(r_i, r_j) \right] \psi = E\psi \qquad (2.1)$$

where the terms in the brackets are the kinetic energy of each electron, the interaction energy between each electron and the nuclei, and finally the interaction energy between each electron, respectively. The solution is the wavefunction, ψ, which is a function of the spatial coordinates of each electron. ψ has 3N dimensions, where N is the number of electrons in the system. This presents a problem if the system is larger than one or two interacting electrons. Model systems of electrolyte-cathode/anode interfaces, such as those studied in this thesis, involve hundreds of atoms and their electrons, making directly solving the Schrodinger equation a poor option. Density Functional Theory (DFT) offers an alternative method to calculating the wavefunction and is the primary method employed in this thesis. DFT explicitly solves for the ground state electron density of a material by mapping the problem of an interacting many-body electronic system onto that of non-interacting electrons in an effective potential.[33]

DFT was developed by Hohenberg and Kohn[34], and is based on two primary theorems:

1. The ground state energy from the Schrodinger Equation is a unique functional of the electron density.

2. The electron density that minimizes the energy of the overall functional is the true electron density corresponding to the full Schrodinger Equations.

With these postulates, Kohn and Sham[35] determined that the electron density can be found by solving a set of equations that only involve a single electron:

$$\left[-\frac{\hbar^2}{2m}\nabla^2 + V(\mathbf{r}) + V_H(\mathbf{r}) + V_{XC}(\mathbf{r}) \right] \psi_i(\mathbf{r}) = \varepsilon_i \psi_i(\mathbf{r}) \tag{2.2}$$

The first two terms in the brackets are the "known" portion of the total energy functional, representing the electron's kinetic energy and the interaction energy between the electron and the atomic nuclei, respectively. $V_H(\mathbf{r})$ is the Hartree potential, which describes the Coulomb repulsion between the electron and the and the total electron density, $\rho(\mathbf{r})$.

$$V_H(\mathbf{r}) = e^2 \int \frac{\rho(\mathbf{r}')}{|\mathbf{r} - \mathbf{r}'|} d^3 r' \tag{2.3}$$

The total electron density also includes the electron being considered by the Kohn-Sham equations, leading to a fictitious self-interaction energy. The correction for this is lumped into the final term in the brackets, $V_{XC}(\mathbf{r})$, representing the exchange and correlation contributions to the Kohn-Sham equations. This term is a functional derivative of the exchange-correlation energy, the exact form of which is unknown.

If the exchange-correlation interaction is known, DFT provides an exact solution to the Schrodinger equation which doesn't rely on any adjustable parameters. In actuality, DFT calculations rely on approximations to reduce computational complexity, the primary of which relate to the exchange-correlation interaction. A number of reliable functional exist, typically based on either the Local Density Approximation (LDA) or the Generalized Gradient Approximation (GGA). However, both of these approximations result in a self-interaction error when treating strongly correlated electron systems, such as transition metals and f-block metals

like the lanthanides and actinides. In these materials, the functionals fail to cancel out a self-interaction term that delocalizes the electrons in partially filled d or f shells. As many cathodes include transition metal oxides, it is necessary to use a modified version of DFT in my calculations, namely DFT+U. DFT+U incorporates an on-site Coulombic correction to more accurately describe the behavior of d and f electrons. The total energy of the system in a DFT+U calculation can be expressed as:

$$E^{DFT+U} = E^{DFT}[\rho] + E^{on-site}\left[\{n_{I,lm\sigma}\}\right] - E^{dc}\left[\{n_{I,lm\sigma}\}\right] \qquad (2.4)$$

where ρ is the total electron density, $n_{I,lm\sigma}$ is the number of electrons on atom I that are occupying orbitals defined by the quantum numbers $lm\sigma$, E^{DFT} is the energy from the traditional DFT calculation, $E^{on-site}$ is the energy due to localized electrons, and E^{dc} corrects for the double counting of terms that occur in both E^{DFT} and $E^{on-site}$. In the Dudarev approach[36], the $E^{on-site}$ and E^{dc} terms can be combined so that the total energy is:

$$E^{DFT+U} = E^{DFT}[\rho] + \sum_{I,lm\sigma} \frac{U_{I,l}}{2}\left(n_{I,lm\sigma} - n_{I,lm\sigma}^2\right). \qquad (2.5)$$

Because U is positive and the occupation n lies between 1 and 0, the summation penalizes non-integrally occupied orbitals by increasing the energy term at that location.

Unfortunately, there is little consensus in the literature on how to select an appropriate value of U for a particular compound. While there are several ways to determine a U value from self-consistent calculations, different methods often yield different U values, and physical properties determined in calculations implementing those values may not agree with experimental results. Other methods treat the U value as a parameter tuned to reproduce known experimental properties. Here too, there are issues: not only does this add an unwanted degree of freedom to the calculation, but a U value that allows for accurate predictions of one physical property may also yield poor agreement with a different property. Therefore, this empirical

approach also leads to many disparate U values. Due to this uncertainty, it is important to carefully explore a variety of U values and select one that best serves the objectives of the calculation.

2.2 Ab initio Molecular Dynamics

Several other methods based on DFT will also be employed. *Ab initio* Molecular Dynamics (AIMD) couples Schrodinger's equation and Newton's laws, and probes the dynamical evolution of a molecular system. DFT is a ground-state calculation. As such, its accuracy is limited to systems at 0 K and 0 time evolution. For many systems - and many of our curiosities about them - it is useful to see how they evolve in time at non-zero temperatures. In short, we want to be able to study the dynamics of "real-world" systems while preserving the accuracy provided by DFT.

Molecular Dynamics (MD) is used to evolve a system of atoms in time in response to the forces acting on each atom. The force acting on atom i is, classically,

$$F_i \; = \; m_i a_i \; = \; m_i \frac{dv_i}{dt} \tag{2.6}$$

The force acting on atom i can be determined directly from the potential energy of the system can be represented as

$$F_i = -\frac{\partial U}{\partial r_i} \tag{2.7}$$

where U is the total potential energy of the system and r_i is the position. Along with the kinetic energy, these relations define the equations of motion of the atoms, which can be written as a system of 6N first order ordinary differential equations

Classical MD uses a user-specified force field, traditionally with fixed atomic charges and radii, to define the potential energy. In aiMD, DFT calculations are used to calculate and update the potential energy of the system on-the-fly at each time step.

2.3 Nudged Elastic Band Method

The Nudged Elastic Band Method (NEB) can be used to find the minimum energy pathway (MEP) between reactants and products, providing information on the rates of various (activated) decomposition reactions. The goal of a Nudged Elastic Band (NEB) calculation is to find the minimum energy path between two local minima on the potential energy surface. This is a study of transitions. Local minima in the potential energy landscape create equilibrium states for the system, and the MEP is the lowest energy path the system can take between those equilibria. The MEP therefore gives us an idea of the minimum energy barriers required to be overcome when transitioning between states. In practice, the minima are the initial and final positions in the calculation. A number of molecular configurations are generated as
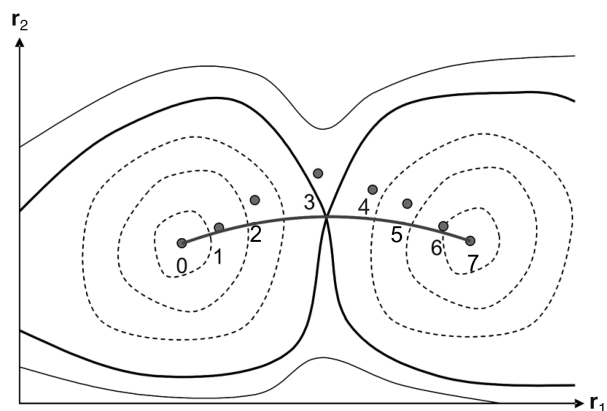
Figure 2.1 2D energy surface with two local minima and the MEP between them. Adapted from Ref 33.

hypothetical steps between the final and initial states. The MEP is defined as where the forces on the images are parallel to the path. The force on the images has two components: the potential energy of the system and a spring force. The force from the potential energy only acts perpendicular to the path. The spring forces only act parallel to the path, and work to keep the images separated. Linear interpolation is used to generate the images in an iterative process.

2.4 Anion Reorientation Time Correlation

Following the procedure from J Smith and DJ Siegel[37] to probe for anion group rotations

in solid electrolytes, the anion reorientation time correlation function was defined as

$$C(t) = \langle \boldsymbol{u}(t + t') \cdot \boldsymbol{u}(t') \rangle \tag{2.8}$$

where $\boldsymbol{u}$ is a unit vector from the anion center of mass to covalently bonded atoms. If there are no rotations, $\boldsymbol{u}(t + t')$ will be the same as $\boldsymbol{u}(t')$, and C(t) will equal 1. When rotations are present, C(t) will decay towards 0. The resulting curves can be fit to an exponential decay to determine the time constant for anion reorientation, τ:

$$C(t) = e^{-\frac{1}{\tau}t} \tag{2.9}$$

2.5 Migration events

Long term, significant cation displacement events in the solid-state were identified using a protocol developed to analyze dynamics in LLZO and glass-forming liquids,[38,39] and which has been successfully used to probe Li migration in glassy solid electrolytes.[37] The functional $h_i(t; a; \Delta t, t_a)$ is defined as:

$$h_i(t; a; \Delta t, t_a) = \prod_{t' = \frac{t_a}{2} - \Delta t}^{t_a/2} \theta(|\boldsymbol{r}_i(t + t') - \boldsymbol{r}_i(t - t')| - a) \tag{2.10}$$

where a is the minimum displacement, set to 2.25Å, t is the time of the event, and $|\boldsymbol{r}_i(t + t') - \boldsymbol{r}_i(t - t')|$ is the displacement of atom i. θ is a Heaviside step function; if the displacement of the atom is greater than a, h_i=1 and if not, h_i=0. Δt is the residence time of the atom preceding and following the event to ensure the displacement is long lived, and is set to 3ps. The total time, t_a, is 9ps, which means the atom has at most 3ps for its displacement. Summing Equation 2.9 at each time t over all ions shows which ions are migrating near simultaneously.

Chapter 3 Modeling ethylene carbonate decomposition on Li₂CoO₂ in the presence of surface magnetism

3.1 Introduction

Li-ion batteries represent the current state of the art in energy storage for portable electronics. No other battery chemistry has been demonstrated to surpass its favorable combination of energy density and cycle life.[1,2,40] Nevertheless, improving the safety of Li-ion batteries remains an important goal.[1,12] For example, the formation of gaseous species resulting from decomposition of the liquid electrolyte can result in the release (i.e., venting) of flammable solvent vapor.[7–11] Previous studies have suggested that gas evolution is impacted by the chemistry of the lithium metal oxide cathode.[4,7–10,12,41] Interactions between the cathode surface and species in the electrolyte could mediate the decomposition of the electrolyte, resulting in gas formation. However, the exact reaction mechanisms responsible for electrolyte decomposition at the cathode surface are not well-understood.
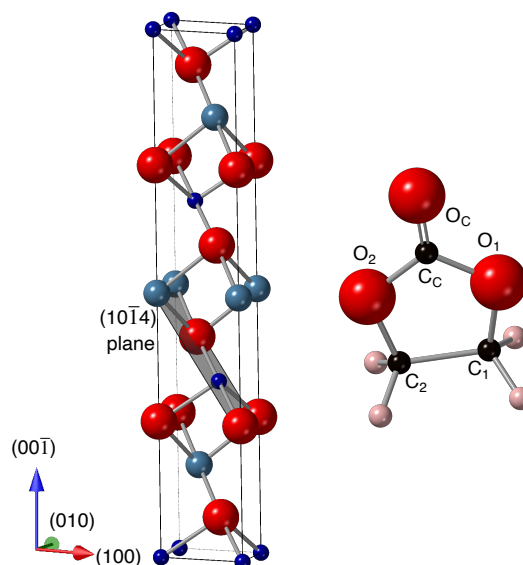
Figure 3.1: Structure of hexagonal LCO (left) and EC (right). The (10-14) plane of LCO is shown within the unit cell. Li, Co, C, H, and O are shown in teal, blue, black, pink, and red, respectively.

The present study investigates how the surface of a $LiCoO_2$ (LCO) cathode could mediate electrolyte decomposition. LCO is an intercalation cathode consisting of alternating layers of CoO_2 and Li ions; Figure 3.1 shows the crystal structure of the hexagonal unit cell. Due to its high energy density, LCO is a common cathode material in commercial batteries, particularly portable electronics.[2] However, in comparing six cathode materials during thermal abuse studies, Roth found that LCO had higher reaction rates, higher enthalpies of reaction, and the lowest onset temperature for gassing reactions.[12] Also, the addition of electrolyte additives were found to yield the smallest improvements in gassing behavior in cells based on LCO. Consequently, the propensity for LCO to facilitate electrolyte gassing has limited its use in some battery applications.

It has been reported that the surfaces of the electrodes can promote electrolyte decomposition.[3,4,7–10] The most prevalent surfaces of LCO crystallites are the (0001), (10$\bar{1}$4), and (01$\bar{1}$2) surfaces.[42–44] Of these, the polar (0001) surface terminating in an oxygen layer has been reported to comprise the largest area fraction. This surface does not participate in Li intercalation.[42] Since Li shuttling during charge/discharge is believed to contribute to electrolyte decomposition, this suggests that electrolyte interactions involving the (0001) surface may not contribute to gassing. Hence, the present study focuses on the (10$\bar{1}$4) surface; this surface is the second lowest in energy, is non-polar, and is expected to contribute to lithium insertion/extraction from the cathode.[43,44] The (10$\bar{1}$4) plane is illustrated within the LCO hexagonal cell in Figure 3.1.

Recent studies have shown that some LCO surfaces exhibit unpaired spins on the surface Co due to the disruption of the structure (i.e., broken bonds) of the oxygen octahedron that would otherwise coordinate Co in bulk LCO.[43,44] In the bulk system, fully coordinated Co^{3+} adopt a low

spin (non-magnetic) state, but Co^{3+} ions at the surface may adopt intermediate or high spin states as a result of broken bonds. In particular, exposed Co^{3+} on the $(10\bar{1}4)$ surface exhibit an intermediate spin state with magnetic moments of ± 2 μ_B.[43–45] Allowing for unpaired spins on the surface Co can lower the surface energy and may contribute to the reactivity of LCO towards electrolytes.

Li-ion batteries use liquid electrolytes consisting of a Li salt, an organic carbonate solvent, and various additives to improve performance. Ethylene carbonate (EC), a commonly used electrolyte solvent, is known to decompose at the anode; these decomposition products are a component in the solid electrolyte interphase (SEI).[4,5] The molecular structure of EC is illustrated in Figure 3.1. Oxidized carbonate species have been found on the cathode surface of LCO-based systems,[2,4,46] which presumably result from decomposition reactions occurring at the electrolyte/electrode interface.

The mechanisms that underlie electrolyte decomposition on LCO surfaces have been investigated in a few previous studies.[46–49] Tebbe et al. conducted a DFT study on the decomposition of EC on the $(10\bar{1}4)$ LCO surface, with and without the addition of other electrolyte molecules. Their study suggested that a high energy barrier to surface mediated decomposition exists in the absence of a strong Lewis Acid, such as PF_5.[47] However, this study did not account for unpaired spins on the electrode surface; furthermore, EC adsorption was limited to surface Co^{3+} ions. Later, Giordano et al. also conducted DFT studies to model EC reactivity with $(10\bar{1}4)$ LCO and other common lithium metal oxide cathodes. Their study examined four potential reaction pathways and assumed a ferromagnetic ordering of surface Co^{3+}. They found EC adsorption and dissociation through deprotonation to be exothermic on LCO.[48] They also found that the driving force for EC dissociation at the surface increased as Li

17

was removed from the electrode. Finally, Tamura et al. used first principles molecular dynamics (FPMD) to study EC on the (11-20) surface of LCO, observing EC adsorption on surface Co^{3+} ions and EC dissociation through ring opening at the surface.[49]

The present study builds on these earlier reports by using classical and first principles techniques to characterize potential gassing reactions in Li-ion batteries. Specifically, the

thermodynamics and kinetics of surface-mediated EC decomposition is probed on the $(10\bar{1}4)$ surface of LCO. Following the methodology of Kumar et al. for solvent adsorption and decomposition, classical Monte Carlo calculations were used to screen hundreds of potential absorption geometries.[50,51] These results, supplemented with geometries from the literature and chemical intuition, were used to down-select more than 30 geometries that were subsequently refined with DFT calculations. The magnetic state of the LCO surface was explicitly taken into account by comparing the adsorption behavior of EC among three different magnetic orderings – non-magnetic, ferromagnetic, and antiferromagnetic – with the antiferromagnetic ordering being the lowest in energy. Surface magnetism was found to have a large impact on the adsorption geometry and the reaction energetics. EC prefers to adsorb at surface Co sites on the non-magnetic surface (the highest energy surface), but prefers Li sites in both ferromagnetic and antiferromagnetic states. In all cases little charge transfer is observed, suggesting that van der Waals and electrostatic interactions dominate.

The thermodynamic driving force for EC decomposition was predicted for eight potential reaction products derived from over 30 different bond breaking scenarios. The most exothermic reaction investigated results in the formation of CO_2 and acetaldehyde (C_2H_4O) with an (exothermic) driving force of 0.85 eV/molecule. The observation of gaseous CO_2 as a reaction product is consistent with prior experiments.[11,46,52,53] In addition, Gauthier et al. have detected

acetal groups at the LCO surface after cycling in an EC-based electrolyte.[46] Nudged Elastic Band (NEB) calculations were used to map out the minimum energy pathway for this decomposition reaction. A relatively large barrier was found, suggesting this reaction will be kinetically limited. As previous studies have reported more rapid solvent decomposition kinetics upon delithiation of LCO and similar lithium metal oxides, it can be hypothesized that a smaller barrier – and a faster decomposition rate – may exist in the (partially) lithiated state.[48,50,54]

3.2 Computational Details

DFT calculations were performed using the Vienna *ab initio* Simulation Package[55–58] (VASP). A plane wave basis set[59] with an energy cut off of 400 eV was used in combination with the projector-augmented wave[60,61] (PAW) method for calculating the interactions between core and valence electrons. Exchange-correlation effects, including dispersion corrections, were treated with the vdw-DF2 functional.[62–66] All calculations were spin-polarized unless otherwise noted. Atomic forces were minimized to a tolerance of 0.04 eV/Å.

Calculations on bulk LCO were performed with a 6x6x6 k-point mesh. It was verified that Co ions in the bulk adopt a low spin state with no individual magnetic moments. Due to well-documented self-interaction errors in the treatment of strongly correlated d shell electrons, a Coulombic correction, U, was applied to the Co ions' d-electrons following the approach of Dudarev.[36] A U value of 3.3 eV was used.[67]

The $(10\bar{1}4)$ surface of LCO has been reported in the literature as a low energy surface.[42–45] This surface also participates in lithium intercalation during battery charge/discharge.[42] While bulk LCO is non-magnetic, it has been noted that under-coordinated Co^{3+} ions on the $(10\bar{1}4)$ surface exhibit non-zero magnetic moments.[43–45,68,69] Our calculations suggest these ions adopt an intermediate spin state with a magnetic moment of ± 2 μ_B, consistent with earlier reports.[43,45]

The presence of surface magnetism has the potential to both lower the surface energy and influence the nature of the interactions between the (magnetic) surface and adsorbed molecules. Consequently, a search over five different surface magnetic configurations was performed; these included: non-magnetic, ferromagnetic, and three antiferromagnetic orderings. Three of these computational cells and their respective isosurfaces of the magnetic spin density are shown in Figure 3.2.

The computational cell used to model solvent decomposition reactions was constructed from a 4x4 expansion of the $(10\bar{1}4)$ surface unit cell. This cell has lateral dimensions of 11.40 Å x 11.27 Å, and a vacuum region of 16.8 Å. These dimensions are sufficient to minimize spurious interactions between periodic surfaces and images of adsorbed solvent molecules. A four-layer slab was used, with the bottom two layers fixed at their bulk-like spacing. In total, each computational cell contained 128 LCO atoms; adsorption and decomposition calculations included an additional 10 atoms from EC. All calculations involving the 4x4 slab (with or without adsorbed molecules) were performed using a single k-point (1x1x1 mesh).

Adsorption energies were determined by: $E_{ads} = E_{slab+EC} - E_{slab} - E_{EC}$, where E_{ads} is the adsorption energy, $E_{slab+EC}$ is the energy of the cell containing the adsorbed solvent molecule on the slab, E_{slab} is the energy of the pristine slab and E_{EC} is the energy of the isolated solvent molecule. The energy of the isolated solvent molecule was calculated in an empty box; this energy was then augmented with the experimental vaporization enthalpy of EC[70], 0.585 eV, to approximate the energy of EC in the liquid phase.

A sub-set of initial candidate adsorption configurations were generated using classical Monte Carlo (MC) simulations, carried out in the Adsorption Module in Materials Studio. These calculations used a fixed surface slab geometry (generated from a prior DFT geometry

optimization), the Universal Force Field[71], and partial charges determined by a Bader Charge[72–75] analysis. As a relatively small molecule, EC has no distinguishing conformations; nevertheless, in the course of the MC calculations the EC molecule was treated either as having a fixed geometry or one that could bend and distort based on energy minimization. The ten lowest energy configurations from both simulation types (fixed or flexible EC) were used as starting structures for subsequent DFT calculations. In addition to the MC-generated geometries, 18 configurations were created by hand and subsequently relaxed via DFT. In total, 38 candidate adsorption configurations for EC on LCO were explored. DFT calculations were performed on these geometries with and without spin polarization. Spin polarized configurations initially assumed ferromagnetic ordering on the surface Co^{3+} ions. The 13 lowest energy and geometrically distinct configurations were further analyzed assuming an anti-ferromagnetic ordering.

Once the most likely intact adsorption configurations for EC were determined, possible decomposition pathways were examined by manually breaking one or two bonds in the EC; every bond in EC was explored in this manner except the double bond between O_C and C_C (see Figure 3.1). Several structures were created for each bond break by either positioning the fragmented ends near oppositely charged atoms on the LCO surface or extending them towards the vacuum region. These initial structures were then relaxed with DFT to determine more realistic configurations and assess their energy with respect to that of the intact structure. In cases were the resulting decomposition products yielded a lower energy than the intact configuration, Nudged Elastic Band[76,77] calculations were used to determine the reaction barrier. Linear interpolation was used to generate five images between the fully intact and fully decomposed state of EC on $(10\bar{1}4)$ LCO. Converging the NEB calculations was challenging due to spurious

(a) Non-magnetic	(b) Ferromagnetic	(c) Antiferromagnetic
Total magnetization= 0	Total magnetization= 32	Total magnetization= 0
Magnetizatin/Co$_{surface}$ = 0 μ_B	Magnetizatin/Co$_{surface}$ = + 2 μ_B	Magnetizatin/Co$_{surface}$ = ± 2 μ_B
E_σ = 0.071 eV/Å^2	E_σ = 0.046 eV/Å^2	E_σ = 0.045 eV/Å^2
E_{mag} = 0 eV	E_{mag} = -0.40 eV/Co$_{surface}$	E_{mag} = -0.42 eV/Co$_{surface}$
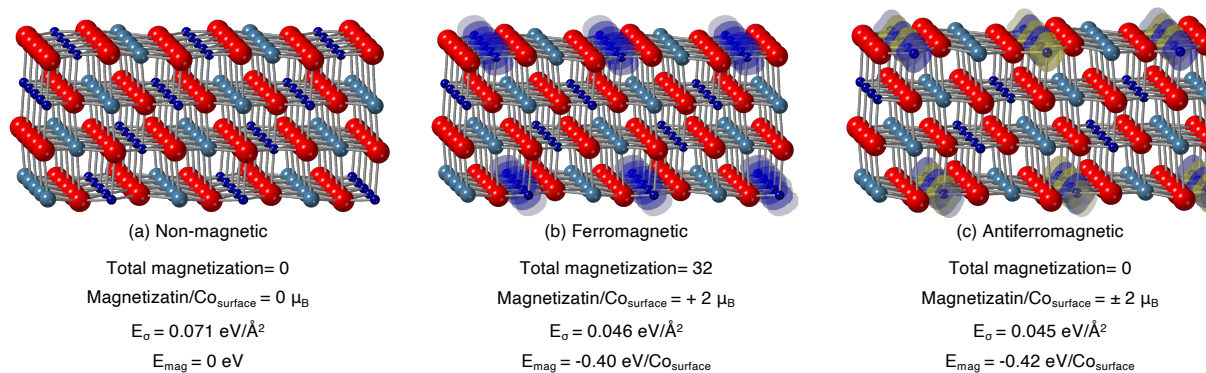
Figure 3.2 Energetic and magnetic properties of $(10\bar{1}4)$ LCO. Isosurfaces of magnetic spin density are shown for the (b) ferromagnetic and (c) antiferromagnetic orderings. E_σ represents the surface energy of the slab, while E_{mag} is the difference between the energies of the magnetic and nonmagnetic slabs, normalized by the number of surface Co contributing to magnetization. The blue (yellow) isosurfaces represent a positive (negative) magnetic moment at that location.

spin flips in the surface Co; spin flips result in sudden increases to the forces and energy of the

impacted images.

3.3 Results

3.3.1 Surface magnetism

To determine the lowest-energy magnetic state of the $(10\bar{1}4)$ surface, surface energies

were evaluated for several magnetic orderings for the outermost Co^{3+}: a non-magnetic state, a

ferromagnetic intermediate spin state, and three antiferromagnetic intermediate spin states.

Figure 3.2 compares the non-magnetic, the ferromagnetic, and the lowest energy

antiferromagnetic configurations on a 4x4 expansion of the surface. The magnetization density

on each atom is displayed using isosurfaces. The magnetization is centered on the surface Co

ions in both intermediate spin configurations. The antiferromagnetic and ferromagnetic

configurations exhibit surface energies that are 37% and 35% lower, respectively, than that of the

non-magnetic surface. These results support the hypothesis that the formation of a distinct

surface spin state stabilizes $(10\bar{1}4)$ LCO. As the antiferromagnetic configuration exhibited the

lowest energy overall, this magnetic configuration is proposed as the most realistic surface model.

3.3.2 Non-dissociative adsorption of EC

To understand how the surface magnetic state impacts the adsorption of EC, adsorption geometries and energies were calculated on each of the non-magnetic, ferromagnetic, and antiferromagnetic surfaces shown in Figure 3.2. The most energetically favorable adsorption geometries for each surface magnetic state are shown in Figure 3.4. In all cases, the most exothermic adsorption sites were found by situating the EC molecule so that the carbonyl and a ring O were positioned over cations on the LCO surface. Altering the magnetic state of the surface impacted both the adsorption energetics and the orientation the adsorbed molecule. The non-magnetic surface resulted in the most exothermic adsorption energies: -0.69 eV vs -0.26 eV and -0.12 eV for the most favorable ferromagnetic and antiferromagnetic cases, respectively. The non-magnetic surface favors EC adsorption at surface Co sites, whereas the magnetic surface

Table 3.1 Adsorption energies for 12 different configurations for each magnetic state studied in this work.

Config. No.	Adsorption Angle and Species	Non-magnetic	FM - IS	FM - LS	AFM - IS	AFM - LS
1	116.1 – Li Li	-0.484	-0.148	-	-0.126	-
2	116.6 – Li Li	-0.482	-0.163	-	-0.123	-
3	115.9 – Li Li	-0.480	-0.140	-	-0.105	-
4	123.8 – Li Li	-0.418	-0.246	-	-0.092	-
5	115.5 – Li Li	-0.472	-0.138	-	-0.079	-
6	126.8 – Li Co	-0.565	-0.269	-0.129	-0.050	-0.008
7	110.4 – Co Co	-0.691	-0.042	-0.080	0.001	0.086
8	110.3 – Co Co	-0.691	-0.105	-0.030	0.001	0.088
9	111.6 – Co Li	-0.584	-0.064	-0.181	0.035	-0.002
10	108.4 – Co Co	-0.695	-0.047	-0.093	0.051	0.081
11	124.8 – Li Co	-0.528	-0.088	-0.110	0.068	0.087
12	122.7 – Co Co	-0.682	-0.143	-0.130	0.083	0.115

| 11 | 124.8 – Li Co | -0.528 | -0.088 | -0.110 | 0.068 | 0.087 |
| 12 | 122.7 – Co Co | -0.682 | -0.143 | -0.130 | 0.083 | 0.115 |
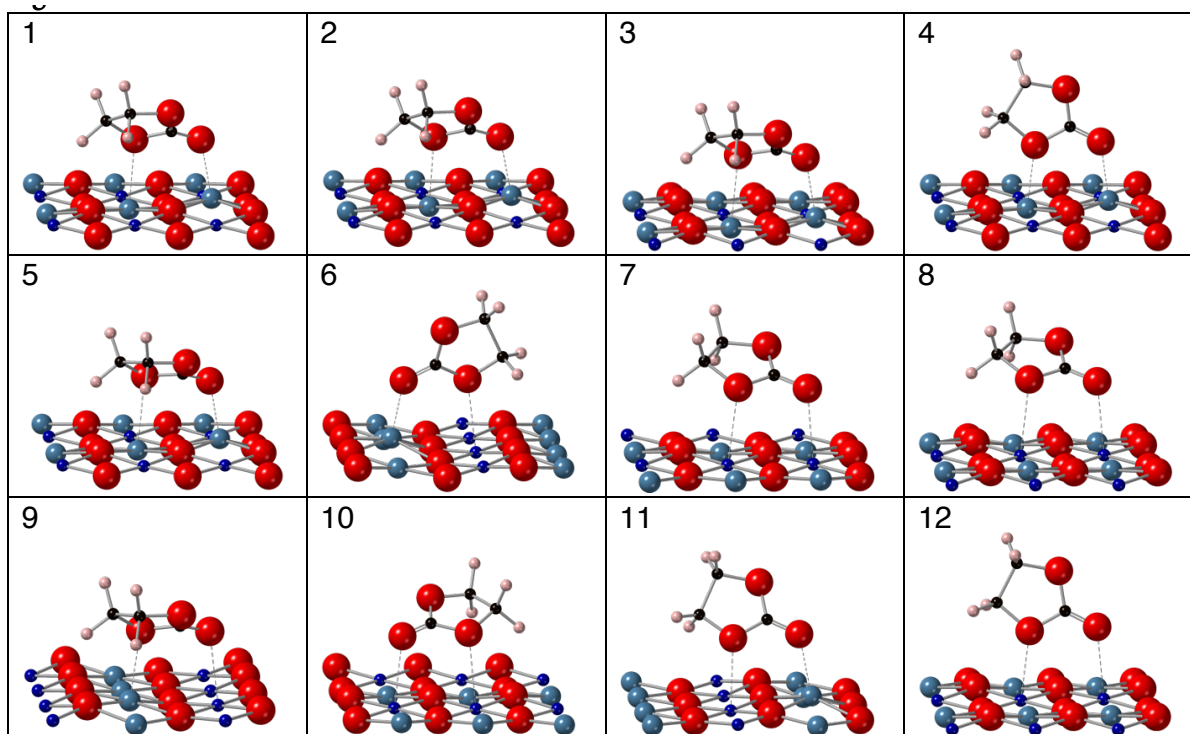
Figure 3.3 EC adsorption configurations enumerated in Table 3.1.

configurations favor adsorption at surface Li. This difference in site preference can be explained
by differences in the electronic structure of the Co ions between the non-magnetic and magnetic
configurations. In the spin polarized, magnetic calculations Co electrons occupy a lower energy
state than in the spin-averaged, non-magnetic calculations. The higher energy of the non-
magnetic configuration implies that these electrons will be more reactive, resulting in a stronger
adsorption energy relative to the magnetic configurations. Since the Li-ions are oxidized
regardless of the magnetic state, their electronic structure is largely unchanged by the
presence/absence of magnetism. The changing site preference for adsorption as a function of spin
polarization primarily reflects changes to the electronic structure of Co ions alone. Hence, the
magnetic state of the slab quantitatively and qualitatively impacts how the EC molecule interacts
with the surface.

Two previous studies of EC adsorption on LCO (10$\bar{1}$4) employed different assumptions about surface magnetism and reported that the carbonyl and/or ring oxygen of EC preferred to adsorb adjacent to surface Co. Tebbe et al. reported an adsorption energy of -1.07 eV/molecule on a non-magnetic surface, which is more exothermic than the -0.69 eV/molecule found here. The discrepancy in these energetics is at least partially due to the use of a different reference energy for EC: here the adsorption energy is evaluated with respect to liquid-phase EC by accounting for the experimental vaporization energy; in contrast, Tebbe et al. used implicit and explicit solvation effects.[47] EC adsorption on the FM surface was also studied by Giordano et al., who reported an adsorption energy of approximately -0.3 eV/molecule. This value is in good agreement with the -0.26 eV/molecule found here.[48] However, that study reported that EC preferred the surface Co site and referenced their adsorption energy with respect to gas-phase EC rather than to the liquid. In the present study, adsorption is observed to be more likely to occur on Li sites when surface magnetism is accounted for. The preference for Li sites may be significant because electrolyte reactions involving surface Li may inhibit Li intercalation or facilitate the formation of Li-carbonate (or other reactions that consume Li).

Additional calculations were conducted to explore whether EC adsorption on an intermediate spin surface Co ion would reinstate the octahedral coordination found for bulk Co, and thereby impose a low spin state. The adsorption energy increased (became more endothermic) when the Co was constrained to a low spin configuration (see Table 3.1) when coordinated by EC. Hence, Co ions on both the ferromagnetic and antiferromagnetic surfaces prefer the intermediate spin configuration even when coordinated by EC. This suggests that the adsorbed O does not interact strongly enough with the surface Co to mimic the bulk octahedral coordination; the adsorption is more likely due to van der Waals and electrostatic interactions.

Charge transfer, as analyzed with Bader Charge calculations, confirmed this hypothesis, as only

0.03 electrons are transferred between the surface and the EC during adsorption.

3.3.3 Decomposition reactions

As the antiferromagnetic surface ordering is the most favorable energetically, the two

lowest-energy antiferromagnetic intermediate spin geometries identified for intact adsorbed EC

were adopted. These geometries are shown Figure 3.4. Starting from these geometries, EC was

subsequently decomposed into several potential reaction products, as described above. The

relaxed geometries of these products are illustrated in Figure 3.5 for the lowest energy intact

geometry. (Decomposition results for the second-most-favorable geometry follow the same

trend.) Upon relaxation, the structures of the candidate products either reverted to an intact EC,

or multiple (additional) bonds broke spontaneously, resulting in the products shown in Figure

3.5. For both initial intact adsorption geometries, two bond breaking events resulted in negative
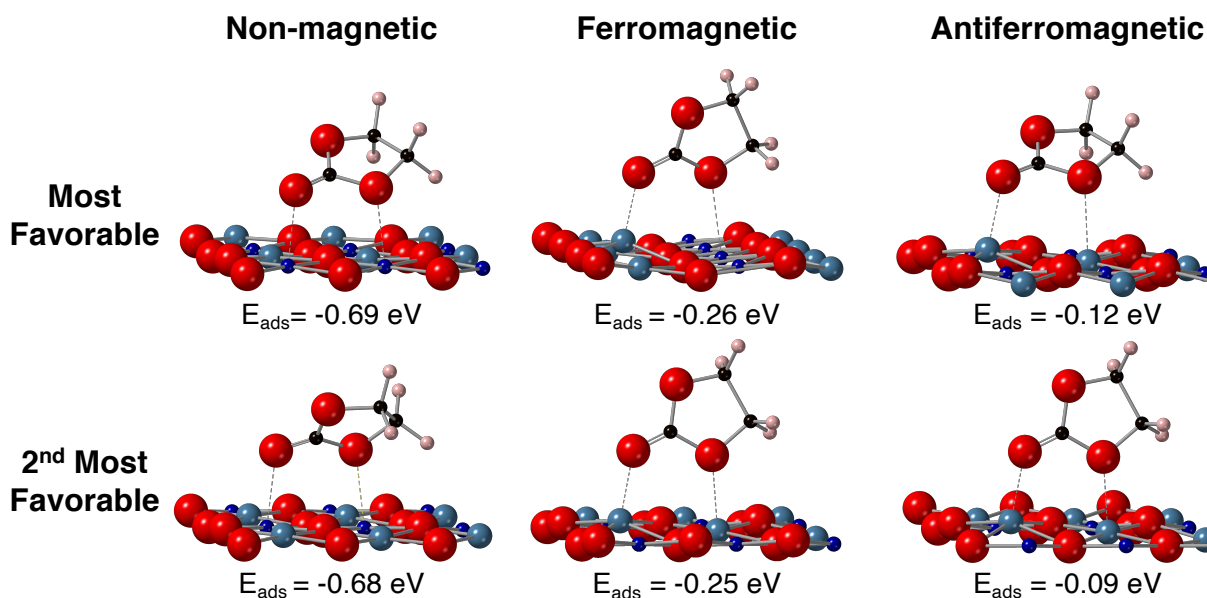
Figure 3.4 The most thermodynamically favorable adsorption geometries for non-magnetic, ferromagnetic, and antiferromagnetic surfaces. E_{ads} is calculated by subtracting the energies of the clean slab and the isolated EC from that of the adsorption geometry. The vaporization enthalpy of EC is also accounted for; thus, E_{ads} represents the adsorption energy with respect to liquid EC.
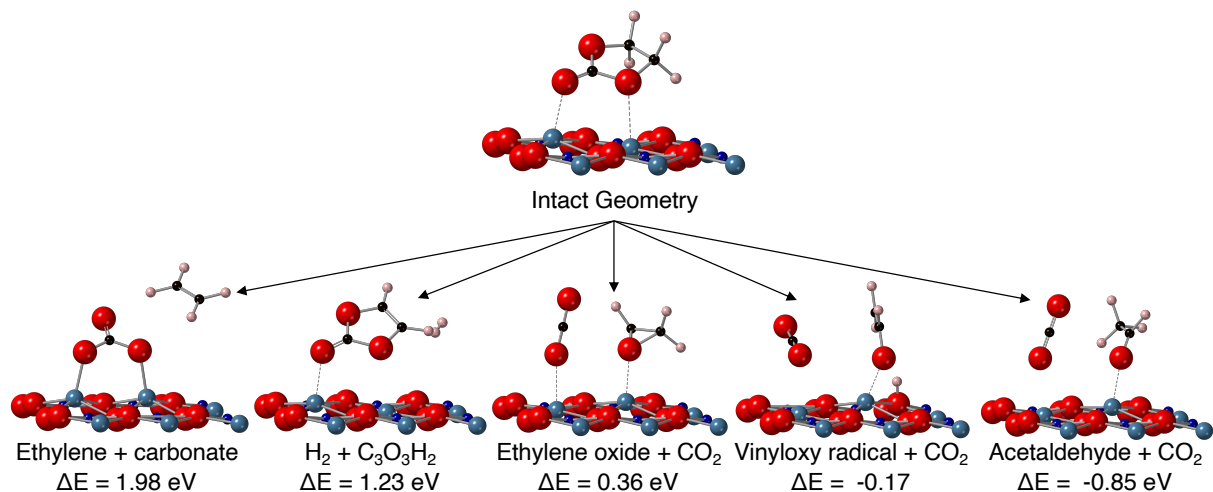
Figure 3.5 Selection of possible decomposed states of EC near $(10\bar{1}4)$ LCO. Five potential decomposition states and the energy difference from the intact state are shown. Two of the five are exothermic, suggesting the decomposition may occur spontaneously.

reaction enthalpies: moving a hydrogen to a surface oxygen (i.e., proton abstraction) resulted in the formation of a vinyloxy radical (C_2H_3O) and CO_2, while breaking the C_1-O_1 bond produced acetaldehyde and CO_2. For both intact adsorption geometries, the formation of acetaldehyde and CO_2 was the most exothermic decomposition reaction, with a reaction energy of -0.85 eV/molecule and -0.83 eV/molecule, respectively. In contrast, the reaction energies for proton abstraction and formation of CO_2 + vinyloxy radical are much less exothermic, -0.17 eV/molecule and -0.13 eV/molecule.

Acetaldehyde and CO_2 are closed shell species that interact weakly with the surface. Importantly, both species are gaseous at or near room temperature, and therefore may contribute to the accumulation of gas in the battery cell. The present findings are in good agreement with experimental data, which report that the main gases produced by electrolyte decomposition in Li-ion batteries are CO_2, CO, and H_2,[11,41,53] and that acetals are commonly identified at the cathode surface.[46]

To determine the impact of the $(10\bar{1}4)$ LCO surface upon EC decomposition, the reaction energy associated with gas-phase decomposition of isolated EC into (isolated) CO_2 and C_2H_4O

was evaluated. This reaction was found to be endothermic, +0.89 eV/molecule, indicating that the LCO surface does play a role in favoring the decomposition reaction.

Prior DFT studies have explored EC decomposition via deprotonation and ring opening pathways.[46–50,54] Tebbe et al. predicted that an EC molecule adsorbed on non-magnetic surface Co decomposed to CO_2 and acetaldehyde with a reaction enthalpy of -0.5 eV.[47] Accounting for surface magnetism, the reaction enthalpy obtained here for the same products, -0.83 to -0.05 eV, is more exothermic. Giordano et al. found that deprotonation occurred with a reaction enthalpy of about -0.3 eV on a ferromagnetic $(10\bar{1}4)$ LCO surface.[48] Conversely, no exothermic deprotonation events were observed in the present study, unless accompanied by additional bond
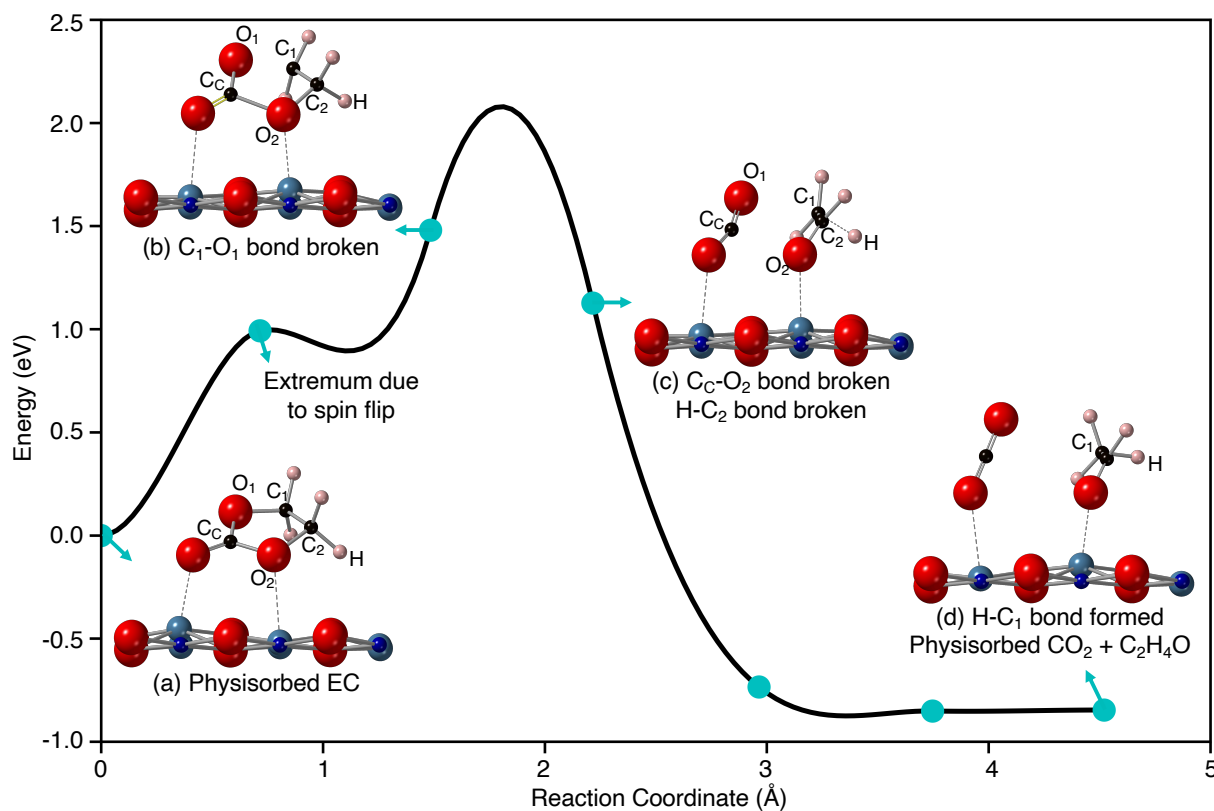
Figure 3.6 Energy profile for the decomposition of physisorbed EC (inset a) into CO_2 and C_2H_4O (acetaldehyde), computed at T = 0 K using the NEB method. The blue circles show the energy of the images used in the NEB calculation. The first maximum (at reaction coordinate ~0.8 Å) is due to spin fluctuations on Co on the inactive (opposite) surface of the slab, and is not related to EC decomposition. Decomposition begins with the breaking of the C_1-O_1 bond (inset b), followed by both the C_C-O_2 and H_1-C_2 bonds, resulting in a physisorbed CO_2 molecule, fragmented C_2H_3O, and an abstracted H (inset c). The abstracted H subsequently bonds with C_1, forming an acetaldehyde molecule that is physisorbed on the surface (inset d).

breaking and the formation of CO_2 and a vinyloxy radical. Additional EC ring opening events were observed with *ab initio* molecular dynamics on the (11-20) surface by Tamura et al., suggesting that other surfaces and ring-opening mechanisms may play a role in EC decomposition.[49]

3.3.4 Reaction barrier

NEB calculations were used to estimate the reaction barrier for the surface mediated decomposition of EC into CO_2 and C_2H_4O. Figure 3.6 shows the energy profile of this reaction, starting from the intact adsorbed molecule (Figure 3.6a) and completing with the formation of CO_2 and acetaldehyde at the surface (Figure 3.6d). (It should be noted that the first local maximum in the energy profile does not necessarily reflect the energetics of this bond breaking event; this maximum primarily results from a simultaneous, unrelated spin flip on two Co ions located in the inactive lower surface of the slab. As previously mentioned, these magnetic instabilities were not uncommon and required careful convergence of the calculations.) The first step in the decomposition pathway is the breaking of the C_1-O_1 bond (Figure 3.6b), which occurs with a barrier < 1.5 eV. The next events in the decomposition reaction involve the breaking of the C_C-O_2 bond and the migration of a H from C_2 to C_1 (Figure 3.6c). The bond breaking portion of this event appears to be the rate limiting step, with a barrier of 2.1 eV. Subsequent bond breaking and formation lowers the energy of the system until the reaction enthalpy of -0.85 eV is reached. The relatively large size of the energy barrier observed here for EC decomposition agrees with previous DFT studies on the non-magnetic surface of LCO, where a similar decomposition pathway with a reaction enthalpy of -0.5 eV and a barrier of 1.81 eV was found.[47] Prior studies report that the barriers for EC decomposition decrease as Li is removed from Li-ion

cathodes.[50,54] Taking the trend reported in Ref. 22 as an example, one may speculate that the present barrier would decrease by 0.5 eV upon delithiation of 1/3 of the Li in LCO.

3.4 Conclusions

Electrolyte gassing remains an important degradation mechanism and safety concern in Li-ion batteries. The present study has used classical and first principles calculations to characterize the thermodynamics and kinetics of electrolyte gassing reactions mediated by the $(10\bar{1}4)$ surface of a $LiCoO_2$ (LCO) cathode. Classical Monte Carlo was used to screen hundreds of potential geometries for ethylene carbonate adsorption (EC) on LCO. Additional geometries described in the literature or derived from chemical intuition were explored. Subsequently, the structure and energetics of more than 30 candidate geometries for EC adsorption were refined using DFT calculations.

Significant qualitative and quantitative differences in adsorption behavior were observed as a function of the magnetic state of the surface. The non-magnetic surface exhibited the most exothermic reaction energetics, and preferentially adsorbed EC on surface Co ions. Nevertheless, the high energy of the non-magnetic surface suggests that it is the least likely magnetic configuration – rather, the anti-ferromagnetic surface was predicted to be the most energetically favorable. With this magnetic ordering EC prefers to adsorb on surface Li sites. Adsorption on surface Co sites have been reported in several studies examining electrolyte decomposition on LCO; our results suggest that decomposition occurs at Li sites when surface magnetism is considered. The preference for Li sites may be significant because electrolyte reactions involving surface Li may inhibit Li intercalation or facilitate reactions that consume Li.

The thermodynamic driving force for EC decomposition was explored for the most favorable adsorption geometries on the antiferromagnetic surface. Over 30 different bond

30

breaking scenarios were investigated with 8 potential reaction products, yielding two exothermic reaction pathways. The most exothermic pathway resulted in the formation of CO_2 and C_2H_4O, in agreement with previous experimental results. The driving force for this reaction, -0.85 eV/molecule; is 1.7 eV/molecule more exothermic than for the same reaction in the gas phase, highlighting the role of the LCO surface in mediating decomposition. Negligible charge transfer between the molecule and the surface suggests the surface catalyzes the decomposition without actively oxidizing the EC.

NEB calculations revealed a barrier of 2.1 eV for the decomposition process, implying that the reaction is kinetically limited. While this reaction pathway is unlikely to be a major contributor to electrolyte gassing in the fully discharged state (corresponding to full lithiation of LCO), it is hypothesized that the rate of decomposition reactions will accelerate as the cathode is (partially) delithiated, i.e., in the charged state.

Chapter 4 Revisiting the Paddlewheel Effect in Li_2SO_4

4.1 Introduction

The challenges associated with stabilizing interface reactions between the liquid electrolyte and the solid electrodes has spurred interest in designing solid electrolytes and all solid-state batteries. As noted in the Introduction, the advantages of SEs include large electrochemical stability windows and a greater resistance to degradation through overheating and mechanical damage. Their stability also enables the use of metal anodes, leading to batteries with gravimetric and volumetric capacities beyond those achievable with Li-ion chemistries.

This chapter describes first principles calculations aimed at elucidating the nature of ionic migration and anion rotation in Li_2SO_4. Although the conductivity of LSO at ambient conditions is not high enough for it to be considered as a candidate for use in batteries, the simplicity of its crystal structure and a wealth of existing of experimental data positions it as an ideal benchmark for understanding the paddlewheel mechanism.

Li_2SO_4 is monoclinic at low temperatures up to its solid-solid phase change at 850 K, at which point it transitions into the high temperature phase (both phases are shown in Figure 4.3).[17,78] In the HT phase the S atoms adopt an FCC lattice, with the Li occupying tetrahedral interstitial positions. A second set of interstitial positions, which are octahedrally coordinated by the anions, are unoccupied. The oxygen atoms in the SO_4 sulfate groups coordinate the central S ions in a tetrahedral geometry. The orientations of the SO_4^{2-} are disordered, and this material is

classified as a disordered or plastic crystal (it has long range order and short range disorder). The

low temperature monoclinic phase is a normal, ordered crystal.

4.2 Computational Details

As done in Chapter 3, the VASP code was used for first principles calculations, with a

planewave basis set and an energy cut off of 475 eV for static calculations and 400 eV for aiMD

calculations.

Four functionals were compared to approximate exchange-correlation effects: the

generalized gradient approximation[59] (GGA), GGA plus an additional van der Waals

component[63] (GGA+vdw-DF2), the strongly constrained and appropriately normed functional[79]

Table 4.1 Comparison of the computed and measured cell shape and volume of high-temperature (LT) and low-temperature (LT) polymorphs of Li_2SO_4 (LSO) for different exchange-correlation functionals. LT computational 0 K results are from Rama Rao et al.,[16] LT experimental results reported at room temperature in Nord,[78] and HT experimental results reported at 908 K are from Nilsson et al.[17]

LT LSO	Functional	V_0 (Å³)	a (Å)	b (Å)	c (Å)	Density (g/cm³)
DFT (0 K)	GGA	12.27	8.32	5.0	8.56	2.13
	GGA+vdw-DF2	12.07	8.32	5.02	8.52	2.16
	SCAN	11.47	8.18	4.9	8.35	2.27
	SCAN+rVV10	11.42	8.16	4.9	8.37	2.28
aiMD Average (900 K)	GGA	12.64	8.49	5.19	8.63	2.06
	GGA+vdw-DF2	12.3	8.7	5.0	8.85	2.12
	SCAN	11.79	8.18	5.02	8.58	2.21
	SCAN+rVV10	11.05	8.35	4.95	8.02	2.36
Results from Literature	GGA	12.42	8.6	5.04	8.41	2.1
	GGA-G06	12.06	8.56	4.98	8.3	2.16
	Experiment	11.7	8.45	4.95	8.21	2.23
HT LSO	Functional	V_0 (Å³)	a (Å)	b (Å)	c (Å)	Density (g/cm³)
aiMD Average (900 K)	GGA	12.7	6.75	7.3	7.24	2.05
	GGA+vdw-DF2	12.3	7.17	6.88	7.0	2.12
	SCAN	11.61	6.84	6.84	6.93	2.25
	SCAN+rVV10	11.34	6.77	6.87	6.84	2.3
Results from Literature	Experiment	12.6	7.07	7.07	7.07	2.065

(SCAN), and SCAN plus an additional van der Waals component[80] (SCAN+rVV10). The GGA and GGA+vdw-DF2 were used in the previous chapter; GGA takes the local density approximation (LDA) that was developed for a uniform electron gas and adds a dependence on the electron density gradient, softening bonds that the LDA 'overbinds.' The PBE formulation of the GGA is known to give balanced descriptions of structures and energies, but it doesn't account for non-bonding intermediate-range van der Waals interactions. The vdw-DF2 semi-local exchange functional replaces a part of the PBE exchange functional and has been shown to improve intermediate interactions such as van der Waals attractions.[62–66] The SCAN meta-GGA functional incorporates the kinetic energy density, allowing it to satisfy all 17 exact constraints appropriate to a semi-local functional at a low additional computation cost.[79] On its own, SCAN captures intermediate-range van der Waals interactions; the addition of rVV10 to SCAN better describes nonlocal and long-range van der Waals interactions.[80] LSO is a nonpolar molecular crystal, so long-range dispersion forces are likely to play a role in describing its bonding.[16]

All four exchange-correlation functionals were critically evaluated with respect to experimental data by predicting the crystalline density, lattice parameters, and bulk modulus for LT and HT LSO. These comparisons were made using static calculations at 0 K and at finite-temperatures using aiMD simulations. As mentioned earlier, one aspect of the debate surrounding the paddlewheel effect involves the relative importance of the lower density of the HT phase (i.e., a volume effect) vs. the contributions of rotational dynamics from the cluster anions. Hence, using an accurate density for the DFT simulations is important. The predicted structural parameters for LSO are reported in Table 4.1, along with computational and experimental results from the literature.[16,17,78]

While no functional performed better in all cases, the GGA+vdw-DF2 had the lowest
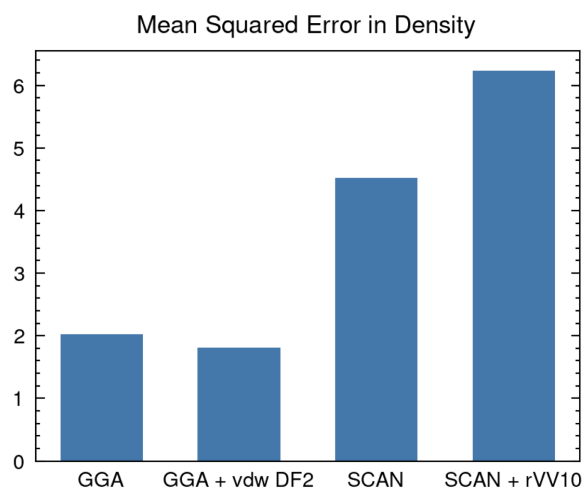
Figure 4.1 Comparison of mean squared error in density calculations for polymorphs of Li2SO4 by functional.

mean squared error in density for both HT and LT phases at 900 K and 300 K, respectively, and was therefore adopted for the remainder of the calculations. The mean squared error per functional is shown in Figure 4.1.

As a further test of the accuracy of DFT to reproduce the experimental densities of LSO, aiMD calculations in the nPT ensemble with a Langevin thermostat was used to allow for thermal expansion/contraction of the lattice at finite temperature. The resulting densities for each phase at several temperatures were compared with experimental data,[17,81–83] Figure 4.2. These data show that the nPT aiMD predictions for the density for LT and HT LSO slightly over-predict the experimental data. In the case of the HT phase, for all temperatures examined the predicted density is approximately 2% larger than the measured values; the change in density vs. temperature (i.e., slope of the density
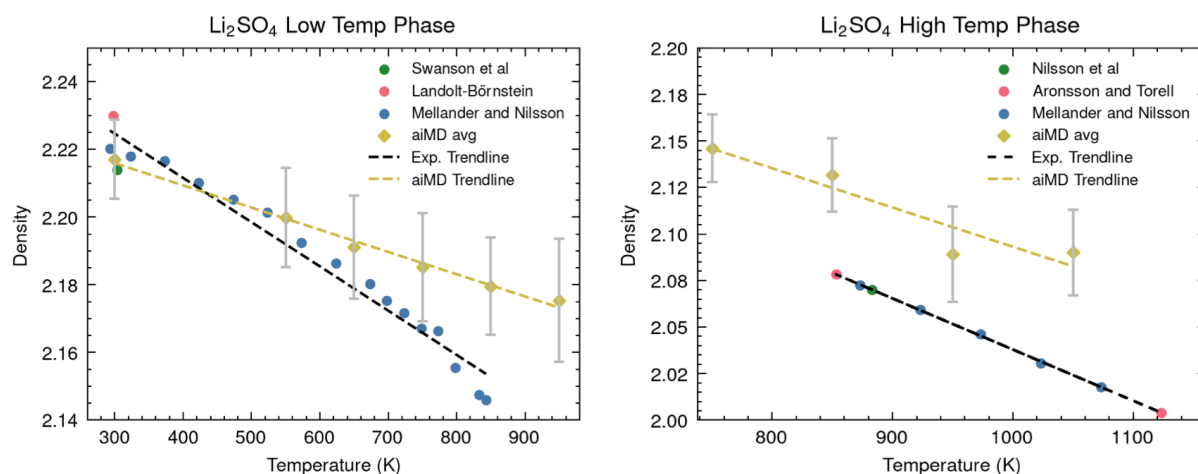
Figure 4.2 Comparison of calculated densities from nPT aiMD as a function of temperature with experimental data.[17,81-83]

Low Temperature Phase
Monoclinic

High Temperature Phase
Face Centered Cubic
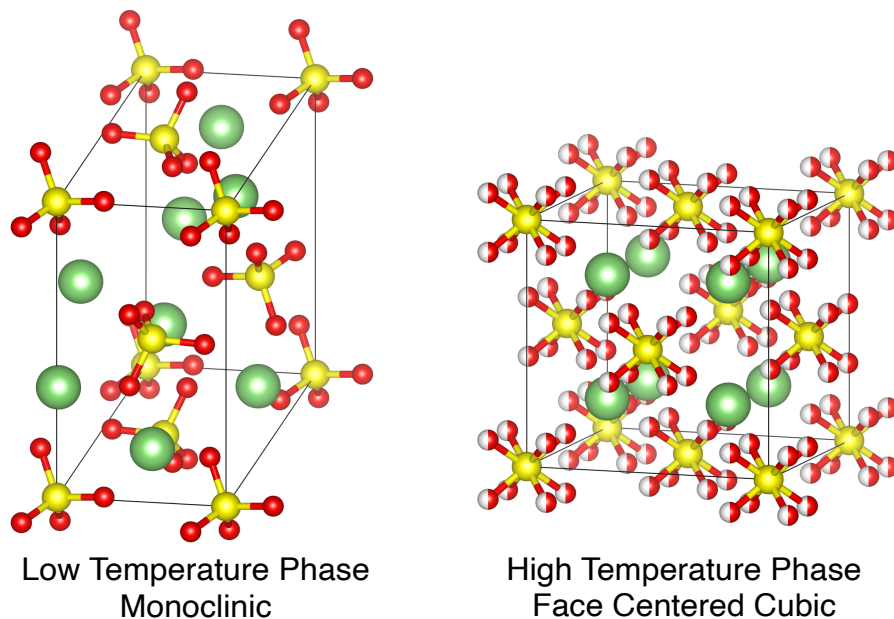
Figure 4.3 Crystal Structure of Li_2SO_4 in high[17] and low[78] temperature phases. Li, oxygen, and sulfur are represented by green, red, and yellow spheres, respectively. Partially filled red spheres in the high temperature phase represent potential oxygen sites.

vs T trend line) is similar for both theory and experiment. In contrast, in the LT phase, these slopes differ more significantly; nevertheless, the magnitude of the difference between theory and experiment is, at high temperatures, similar to that of the HT phase, i.e., theory overestimates the density by ~2%. While these calculational errors are reasonable for both phases of LSO, in all subsequent aiMD simulations we chose to adopt the experimentally-determined cell volumes. While this introduces an additional empirical parameter, the density is likely to impact the ability of the anions to rotate and is therefore an important parameter for which to minimize errors with respect to experiment.

The crystal structure of HT LSO, shown in Figure 4.3, exhibits partially-occupied oxygen sites, as determined by X-ray diffraction.[17] These partial occupancies reflect the presence of orientational disorder for the anions, which could be either static or dynamic in nature. Atomistic calculations do not allow for partial atomic occupancies, so the initial positions for each oxygen atom were set manually at the outset of each simulation. In the course of benchmarking the unit

36

cell, the bulk modulus of HT Li_2SO_4 was calculated according to the Birch-Murnaghan equation of state[84] and compared with the experimental bulk modulus extrapolated to 0 K.[81] The average percent error in the calculated bulk modulus 44%. This discrepancy prompted the reexamination of the orientation of the sulfate tetrahedra in the model. The simulation cell consisted of 4 formula units of Li_2SO_4 and orientations of the sulfate anions were artificially disordered by either: rotating one sulfate group, shortening one S-O bond in a sulfate group, or by using the structure generated by running 3ps of aiMD with GGA or GGA+vdw-DF2. The disordered structures were relaxed with DFT, and the average percent error in the bulk modulus dropped to 28%. While this is still a high error, part of that is likely due to the audacity of comparing a value calculated at 0 K to a trend seen in 900-1100 K and then extrapolated to 0 K. The disordered model was used for further benchmarking the exchange-correlation functionals.

In the aiMD calculations, a large simulation cell was used to reduce spurious interactions between periodic images and maximize the opportunities to observe Li migration events. The supercell consisted of 32 formula units of LSO, for a total of 224 atoms. One neutral Li was removed from the supercell to create a vacancy which could mediate cation migration. After 10 ps of equilibration, 80 ps of aiMD time was simulated to collect data on the dynamics of the system. The LT phase was simulated at 550 K, 650 K, 750 K and 850 K. The HT phase was simulated at 850 K, 950 K, and 1050 K. The low (high) temperature phase was also simulated at 100 K above (below) the transition temperature of 850 K, i.e., 950 K (750 K).

4.3 Results

The anion reorientation time-correlation function, C(t), was calculated according to Equation 2.8 for aiMD runs of both Li_2SO_4 polymorphs at all simulated temperatures, and plotted in Figure 4.4. Results for the LT phase show that C(t) maintains a nearly-constant value

of unity for all simulated times, consistent with little to no anion rotations at any temperature at or below the transition temperature, 850 K. Such an observation of negligible disordering of the sulfate ions orientations is consistent with experiments.[16]

In contrast, the calculated C(t) for the HT phase exhibits a rapid decay to values close to zero over a relatively short 20 ps timescale. Additionally, the rate of decay of C(t) increases with increasing temperature. This behavior implies that reorientations or rotations of the tetrahedral anions occur over the course of the simulation. Furthermore, when the LT phase was simulated at a temperature 100 K above the transition temperature, its C(t) exhibited a decay suggestive of anion rotations similar to that of the high temperature phase at the transition temperature. Likewise, when the HT phase was simulated at a temperature that was 100 K below the transition temperature, little to no rotations were observed. This suggests that anion rotations 'turn on' near the transition temperature.

Migration events for Li-ions were detected by analyzing the atom positions over time using Equation 2.10. The Heaviside function was attuned to a displacement threshold of 2.25 A and a residence time of 3 ps[37] to ensure events are long-lived and show a sufficiently-large change of cation position consistent with a migration event. The results from this analysis are shown in Figure 4.5. The data show that the LT phase exhibits no migration events at 450 K, even when the displacement threshold was shortened to 1.6 A. At higher temperatures of 650 to 850 K, some Li migration events begin to occur, but they
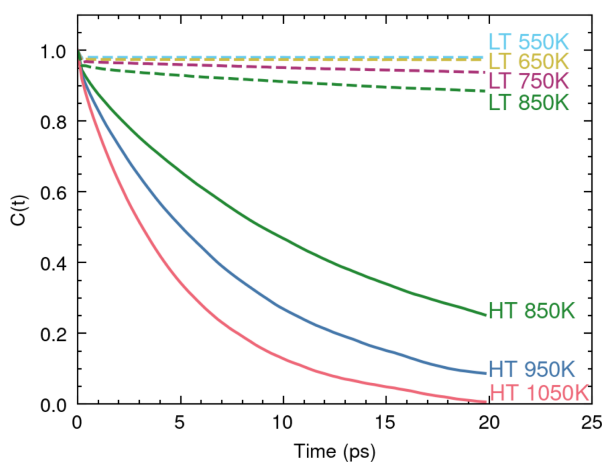
Figure 4.4 Reorientation correlation time of SO_4^{2-} in LSO polymorphs.
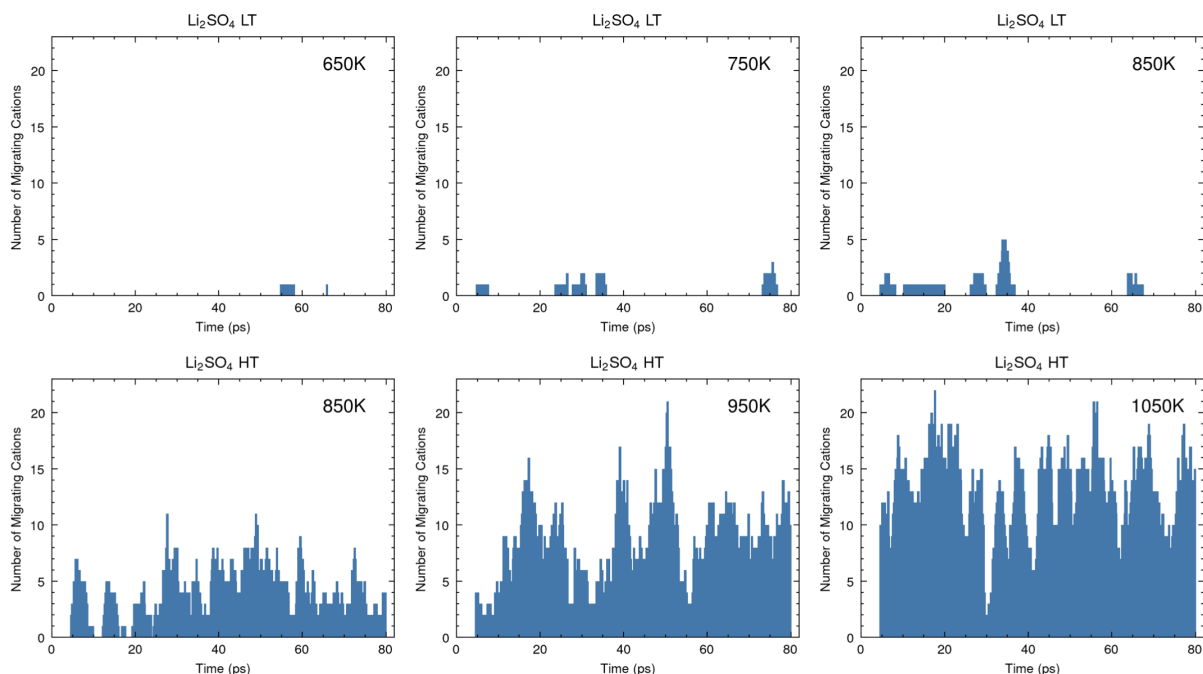
Figure 4.5 Detection of Li-ion migration events in LT and HT LSO as a function of simulation time and simulation temperature.

are few in number, and these events generally involve 1 or 2 Li-ions.

In contrast, the HT phase shows numerous migration events at all temperatures, with each event often involving upwards of 5 Li^+ moving simultaneously. The large number of events, and their concerted nature, differ markedly from that of the LT phase, and is consistent with experimental data showing that the HT phase exhibits a significantly larger ionic conductivity.

The right panel of Figure 4.6 shows an Arrhenius plot based on the Mean Squared Displacement (MSD) data for Li migration in the high temperature phase. A similar plot could not be calculated for the LT phase due to a dearth of migration events and poor MSD statistics. The calculated activation energy for Li^+ migration is 0.48 eV, which agrees with experimental results, which range from 0.34eV to 0.53 in the literature.[15,19,85,86] The C(t) data was used to calculate a time constant, τ, for anion reorientation by fitting to Equation 2.9. At 1050 K, the time constant was 5 ps, on the same order to the 1ps reorientation time reported near melt (1133
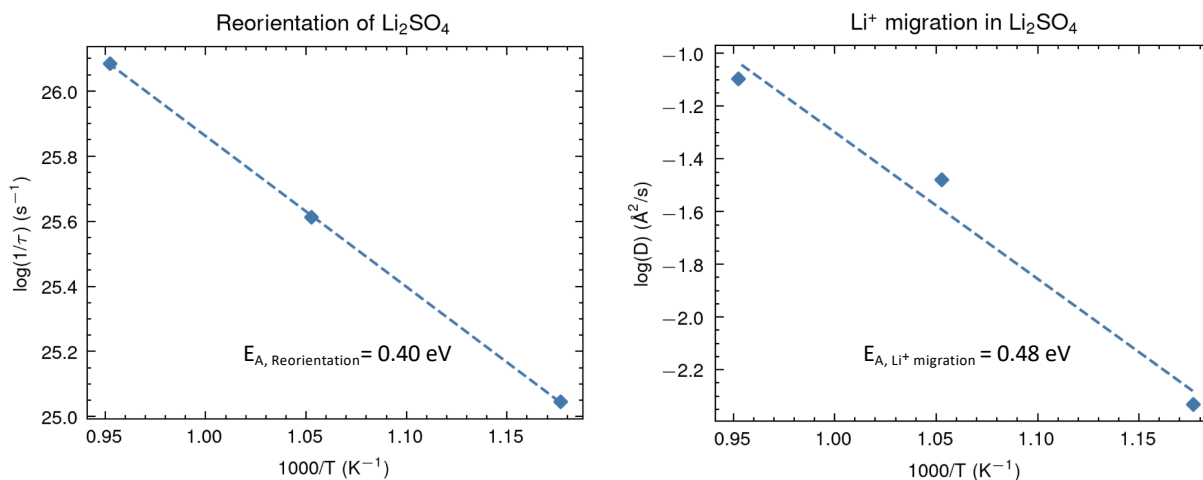
Figure 4.6 Arrhenius plots and activation energies for SO_4^{2-} reorientations (left) and Li^+ migration (right) in HT LSO.

K).[85] The slope of an Arrhenius plot of τ vs inverse temperature yielded a reorientation activation
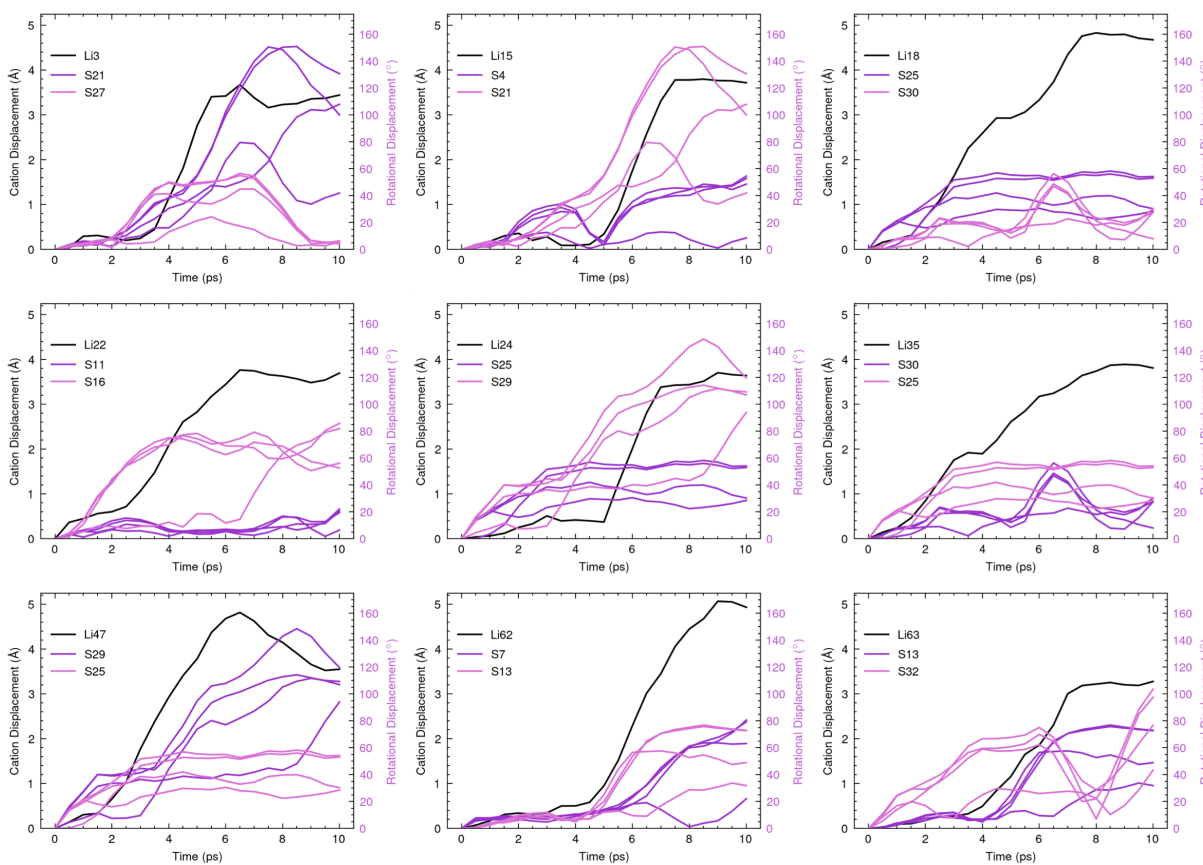
Figure 4.7 Correlation between Li^+ displacements (black lines) and the rotational displacements exhibited by two nearest-neighbor sulfates, each with four reorienting O atoms (purple lines) for the migration event beginning at 22.7ps.

40

energy of 0.4 eV (Figure 4.6 left panel). This value also agrees with experimental measurements, which report an activation energy of 0.43eV for anion reorientations.[87] Importantly, both simulations and experiments agree that Li^+ migration events and SO_4^{2-} reorientations have similar activation energies. These energetic similarities would be expected if the occurrence of these events were correlated.

Figure 4.7 examines potential correlations in time and in space between Li-ion hops and anion reorientations in HT LSO. There, cation displacements are plotted vs rotational displacements of two neighboring SO_4^{2-} anions over a 10 ps time window for the aiMD run conducted at 850 K. The time window begins at 22.7 ps. The plots confirm that the identified migrating cations exhibit displacements over 2.5A and do not return to their previous site over during the 10ps event time. Each cation displacement is paired with the rotational displacement of two nearest-neighbor sulfate groups (identified by the index of the central S atom); each S-O vector is represented by a purple line (light purple for one sulfate, dark purple for the second). Many of these displacement events demonstrate the time and space correlation between cation migration and anion reorientation that typify the paddlewheel mechanism. In the top left plot, the displacement of "Li3" is plotted alongside "S21" and "S27." Correlation is
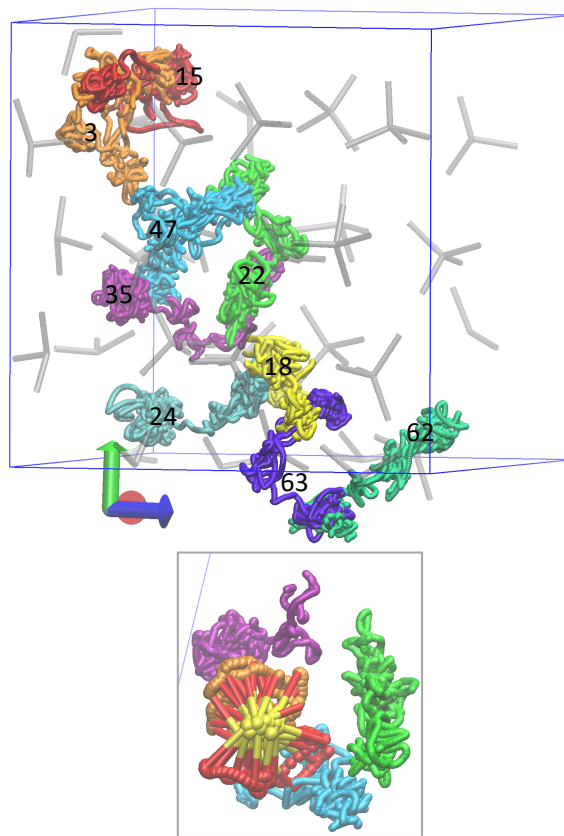
Figure 4.8 Trajectory of Li^+ migration event from Figure 4.7.

shown between Li3 and S21, marked by the sharp increase in displacements between 4-6 ps of event time. The reorientations of S21 are large, displacing as much as 150 degrees, and it does not return to its time=0 energy basin. The other nearest-neighbor sulfate, S27, exhibits rotational displacements of at maximum 60 degrees and does return to its original orientation by the end of the event time. There does not appear to be correlation between the less-rotationally-displacing S27 and Li3. Of the remaining plots, "Li15," "Li22," "Li24," and "Li47" also show time correlation between Li+ migration and the large rotational displacements of nearest neighbor anions, suggesting the paddlewheel mechanism is active in these cases.

As further confirmation of the paddlewheel mechanism in Li2SO4, the trajectories the migrating Li^+ ions from the event depicted in Figure 4.7 are shown during the 10 ps event time window in Figure 4.8. The trajectories display how the Li hop from one site to the next in a chain of motion. While the Li^+ prefer to sit in the tetrahedral sites, they do pass through the octahedral sites while migrating. The inset shows an example of an SO_4^{2-} rotating in concert with a neighboring Li^+ migration. Videos of the trajectories confirm the correlated motion between the migrating cations and rotating anions.

4.4 Conclusion

There is a notable change in the C(t) of the SO_4^{2-} anions from the low temperature to the high temperature phase of Li_2SO_4, suggesting the change of phase does allow for anion reorientation. This is further supported by aiMD trajectories and the rotational displacement plots. Furthermore, there were negligible Li^+ migration events in the low temperature phase during the 80ps of runtime, regardless of simulation temperature, but all high temperature phase simulations included dozens of events involving multiple Li^+ ions. This follows experimental findings,[14] were Li^+ conduction increases by multiple orders of magnitude at the phase transition.

Furthermore, many of the migrating Li^+ move in tandem with the rotations of nearby SO_4^{2-} anions, as shown in both Figure 4.7 and in the trajectory plots of Figure 4.8. This confirms coordinated motion of the ion and rotating anion, indicating that the paddlewheel mechanism is active in this phase.

This material represents the conception of the paddlewheel mechanism and decades of debate. This work finds strong evidence of coordination between migrating cations and large reorientations of the neighboring anions in HT LSO. The confirmation of the ionic conduction mechanism may allow researchers to move forward with confidence in the impact of the paddlewheel effect on ion conduction, and aid in the prediction of novel paddlewheel materials.

Chapter 5 Exploring the Paddlewheel Effect in Na_2SO_4 and K_2SO_4

5.1 Introduction

The previous chapter saw that the paddlewheel mechanism is active in HT Li_2SO_4, with this phase exhibiting a high ionic conductivity of ~1 S cm^{-1} at 1000 K. Some other sulfates, such as $LiAgSO_4$ and $LiNaSO_4$, also reach high ionic conductivities in their high temperature phases,[88] but this is not a universal phenomenon. For example, HT Na_2SO_4 and HT K_2SO_4 are noteworthy in that neither are fast ion conductors; in the high temperature phase, NSO has a conductivity of $9*10^{-4}$ Scm^{-1} at 833 K and KSO similarly has conductivities on the order of 10^{-4} in its high temperature phase.[85] This is surprising, given that Na and K are both alkali metals that lie within the same column of the period table as Li, suggesting similar electronic structure. Both Na_2SO_4 and K_2SO_4 also exhibit a low-to-high temperature polymorphic phase transformation, similar to that for Li_2SO_4, where the HT phase has a higher molar volume and orientational disorder in the sulfate tetrahedra. So the question remains: why is HT LSO a good ionic conductor, while the analogous Na- and K-based sulfates are not? This chapter seeks to provide an explanation for these differences using first-principles calculations.

The low temperature phase of NSO is orthorhombic, and is illustrated in the upper left quadrant of Figure 5.1. This LT phase is stable at atmospheric pressure up to 470 K.[29,89,90] Upon further heating, the material goes through several solid-solid phase transformations over a narrow range of temperatures until finally transforming into the HT hexagonal structure, which is stable above 513 K. The HT phase melts at 1157 K.[29,89,90] The SO_4^{2-} tetrahedra are known to

44
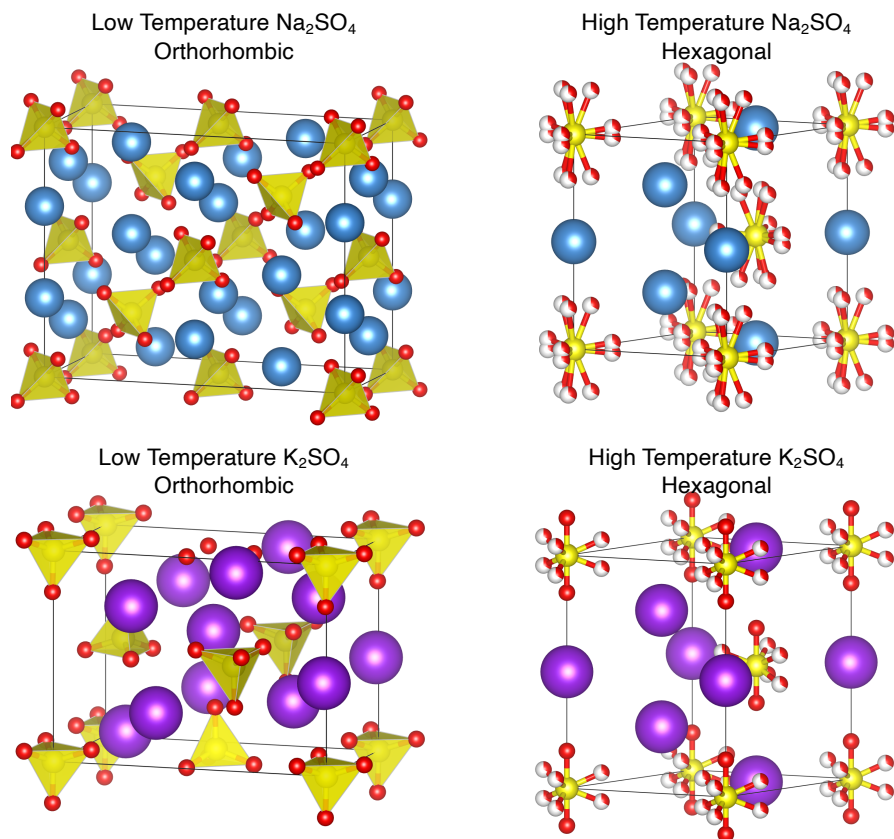
Figure 5.1 Structure of high and low temperature Na_2SO_4 and K_2SO_4. The partially filled spheres in the HT phases represent the possible oxygen sites. Na, K, S, and O are represented by blue, purple, yellow, and red spheres, respectively.

exhibit some form of orientational disorder in the HT hexagonal phase; the crystal structure in Figure 5.1 showcases the disorder as partially filled spheres. Previous studies have found that close to the transition temperature, the sulfate anions exhibit an edge model orientation, where each tetrahedra has one edge parallel and one edge perpendicular to the c-axis.[91] At higher temperatures the c-axis expands more than the a-axis, and the tetrahedra adopt an apex model orientation, where one tetrahedron face is parallel to the c-axis, with an equal probability of its corresponding apex pointing up or down.[29] Figure 5.2 gives an example of the edge and apex model in K_2SO_4, which goes through a similar structural transition in the HT phase.[92]

Single crystal x-ray diffraction on HT NSO was unable to determine if the orientational disorder of the anions is static or dynamic.[29] Static disorder implies that the anion orientation

45

differs from site to site within the crystal. Dynamic disorder implies that the tetrahedra rotate (independently) in time, similar to what was observed in the previous chapter for LSO.

The phase evolution in KSO with respect to temperature is very similar to that of NSO. KSO also transitions from an orthorhombic LT phase to an anion-disordered, hexagonal high temperature phase, albeit at a much higher transition temperature (~860 K) than NSO (~513 K).[92] Similarly, there is ambiguity in the literature as to whether the disorder in the sulfate orientations of KSO is static or dynamic.[92–96]

In the literature it has been postulated that Na_2SO_4 and K_2SO_4 do not exhibit anion rotations (i.e., are not plastic crystals), and the absence of these anion dynamics suppresses their ionic conductivity.

Plastic crystals are a group of molecular crystals where the center of mass of the molecules forms a regular crystal lattice, but the molecules themselves are orientationally and dynamically disordered.[97] A proposed indicator of a plastic crystal behavior is that the enthalpy
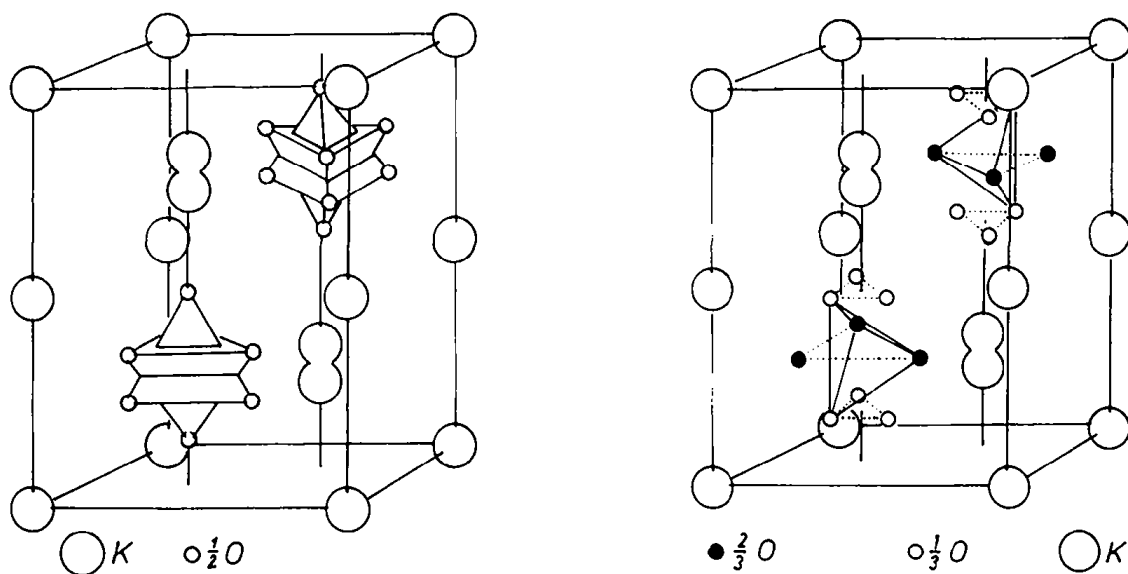
Figure 5.2 Apex (left) and edge (right) model of sulfate tetrahedra orientations in HT K_2SO_4. The sulfate anions in HT N_2SO_4 adopt similar orientations. Reproduced from Ref 92 with permission of the International Union of Crystallography.

of melting of the HT solid phase, ΔH_f, is less than the solid-state transition enthalpy to the HT

plastic phase, ΔH_{S-S}. This trend is true for Li_2SO_4; $\Delta H_f = 9.0$ kJ mol^{-1} while $\Delta H_{S-S} = 24.8$ kJ mol^{-1}, but not NSO (KSO), where $\Delta H_f = 21$ kJ mol^{-1} (30 kJ mol^{-1}) and $\Delta H_{S-S} = 7$ kJ mol^{-1} (8 kJ mol^{-1}).[23,88,94,98]

Börjesson and Torell measured the Raman spectra of the high- and low-conducting

sulfates.[99,100] They found that the widths of the internal sulfate modes, denoted $v_1 - v_4$ in Figure

5.3, are broader in a fast-conducting sulfate such as $LiNaSO_4$ than in the low-conducting sulfate,

Na_2SO_4. They also note that the isotropic (polarized) component of the v_1 node is due to

vibrational relaxation, while the anisotropic (depolarized) component is due to both the

vibrational and reorientational relaxation. In other words, reorientations are present if the

anisotropic component is greater than the isotropic. They observed this trend in Li_2SO_4 and

$LiNaSO_4$, but not in Na_2SO_4 (Figure 5.3), and therefore proposed that the fast ion conductors are

also rotor phases, while low conductivity sulfates are not.

In contrast, Eysel et al.[29] studied a single crystal of Na2SO4 with x-ray diffraction, and

were unable to discern if the disorder was static or dynamic. Later, Choi and Lockwood[96]

Figure 5.3 Raman spectra for high and low conducting sulfates. Adapted from Refs 99-100.

47

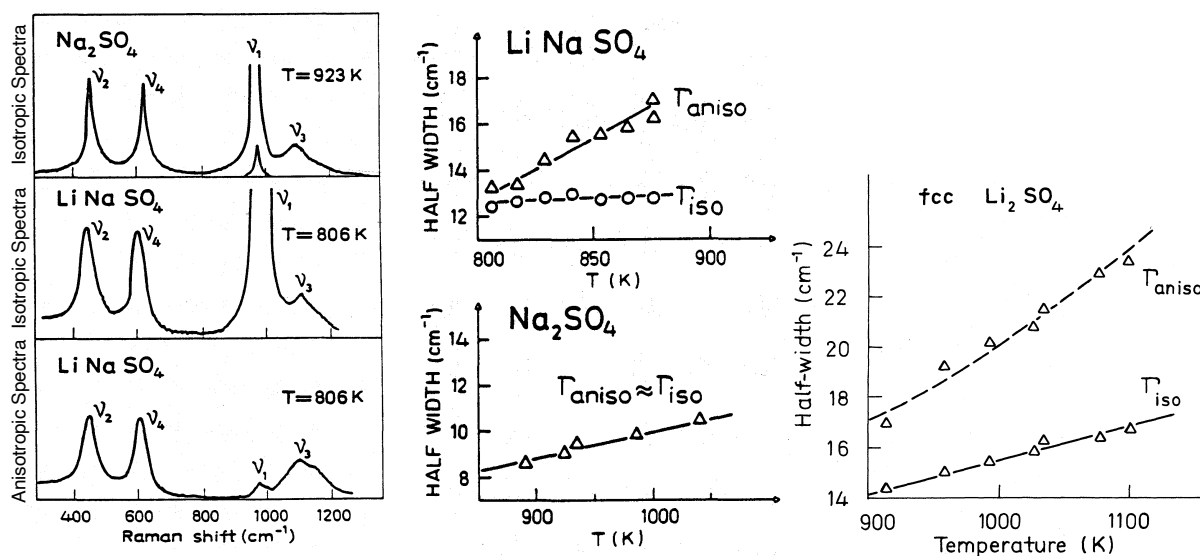suggest that the external lattice mode spectrum of HT Na2SO4 is more similar to the broad wing seen in HT LSO, which is a cubic fast ion conductor, than the hexagonal KSO, which shows distinct lattice modes even near melt. They argue that this is due to the cation motion and that HT NSO is in a 'quasi-fast-ion conducting state,' though they are unable to confirm the paddlewheel mechanism, while also referring to K2SO4 as a 'normal ionic solid.' Both neutron diffraction[92] and power diffraction[101] studies on K2SO4 have been used to argue that the HT phase exhibits dynamic disorder, though not complete rotational freedom. Conversely, other studies review the same data but ascribe to a static disorder model.[93]

5.2 Computational Details

NSO and KSO were examined using the same methodology that was applied in chapter 4 to study Li_2SO_4. The LT phase of NSO was simulated with aiMD at 350, 450, and 550 K while the high temperature phase was modeled at 550, 650, 750, and 850 K (recall that the transition temperature of NSO is 513 K). Only the high temperature phase of KSO was studied, with 80 ps of aiMD at 950 K (transition temperature = 860 K). The unit cell of hexagonal HT NSO and KSO contains 14 atoms. To create a cell with the same number of atoms as used in the LSO study, the unit cell was replicated into a supercell of 224 atoms. One metal cation was removed from each polymorph to introduce a vacation and hopefully stimulate cation migration.

5.3 Results

The anion orientation auto-correlation function (C(t), Equation 2.8) was calculated from the aiMD trajectories to characterize rotations in the sulfate anions. The results of these analyses are shown in the left panel of Figure 5.4 for both LT NSO, HT NSO, and HT KSO. As in LT LSO, C(t) for the LT NSO polymorph remains near 1 for all temperatures studied, indicating

negligible anion reorientations in this phase. However, in the HT phase the rapid decay of C(t) with increasing simulation time and temperature indicates that the anions' orientations are disordered in this phase. This disordering is present even at lower temperatures such as 550 K, which is just slightly above the transition temperature. Our simulations clarify the ambiguity in the experimental literature regarding the nature of anion disorder in NSO: our first-principles calculations clearly indicate the that the sulfate anions in HT NSO are dynamically disordered.

Regarding HT KSO, the left panel of Figure 5.4 plots the anion reorientation time correlation functional for HT KSO at 950 K as a dotted green line. The rapid decay of C(t) to zero shows that the anions in this phase also disorder over pico-second timescales. The right-hand panel of Figure 5.4 C(t) for the HT polymorphs of LSO, NSO, and KSO are compared at temperatures that are approximately 100 K above their respective transition temperatures. This data shows that each material exhibits significant anion rotations above their transition temperatures, suggesting similar anion dynamics are present across all compositions in their respective HT phases.

The time constants for anion reorientation, τ, were calculated for HT NSO using Equation 2.9 and displayed in an Arrhenius plot to determine the activation energy of dynamic SO_4^{2-} reorientations, Figure 5.5. The calculated value of 0.2 eV is a factor of two less than what was found for HT LSO, suggesting that rotations in this material are even more facile than in HT LSO, that latter of which is an acknowledged rotor phase. This behavior is confirmed by comparing the autocorrelation data for both HT phases at the common temperature of 850 K (Figures 4.4 and 5.4), which shows that disordering in NSO occurs more rapidly than in LSO. Unfortunately, our attempts to measure the mean squared displacement data for Na-ion migration in NSO uncovered too few cation migration events to accurately predict the activation energy for
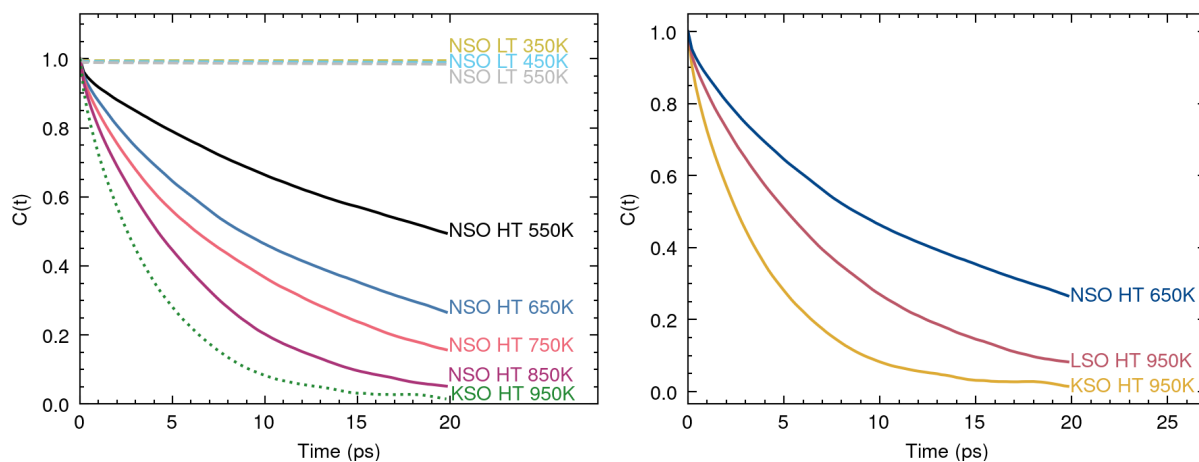
Figure 5.4 Reorientation time correlation function for SO_4^{2-} in NSO and KSO polymorphs. The left panel plots C(t) for all simulated polymorphs of Na2SO4 and K2SO4. The left panel compares C(t) for HT LSO, NSO, and KSO at roughly 100 K above their respective transition temperatures.

cation diffusion. Hence, a comparison between the migration energy barriers of Na-ions and the rotational energy barriers of the sulfate anions in HT NSO was not possible. (We recall that these barriers were similar in the case of HT LSO.)

Figure 5.6 quantifies the occurrence of long-lived cation migration events in HT KSO and in both the LT and HT polymorphs of NSO, as determined by Equation 2.10. The low temperature phase of NSO showed no Na-ion migration events, which agrees with its negligible ionic conductivity as determined experimentally.[102–104] In contrast, in the high temperature phase, several migration events are observed at 850 K, many involving 2-3 Na^+ cations. Nevertheless, these migration events are significantly less frequent than those seen in HT LSO at 850 K (compare Figure 4.5), which often included the concerted motion of up to 8-10 Li-ions in a given event. Migration events in HT KSO are also infrequent: fewer events occur in KSO at 950
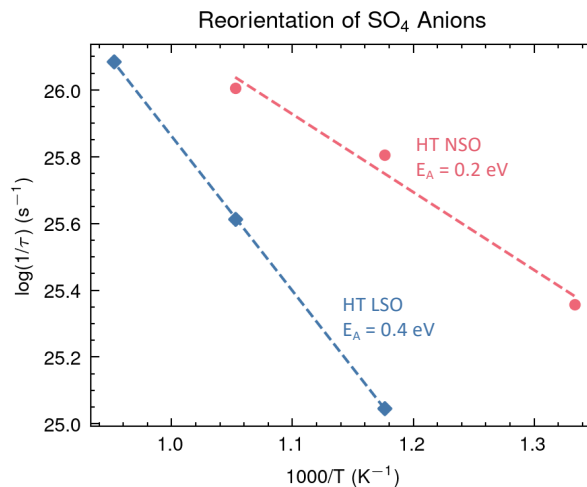
Figure 5.5 Activation energy of anion reorientations in HT NSO and LSO.

K compared to NSO at the lower temperature of 850 K. These trends are consistent with the experimental data of ionic conductivity in these materials.[15]

It is noteworthy that the anion rotations observed in our simulations for HT NSO do not coincide with this material being a fast ionic conductor. This behavior differs from what was observed in our aiMD simulations for HT LSO, which exhibits both dynamical disordering of the anions and high ionic conductivity. Experimentally, the conductivity of these two phases differ by 4 orders of magnitude at 900 K. These differences are especially striking given that at the common temperature of 850 K, C(t) for these phases exhibits a steeper decay (implying more rapid anion disordering) for HT NSO than for HT LSO. These observations raise the question: if both HT phases of LSO and NSO exhibit anion rotations, why is LSO a fast ion conductor whereas NSO is not?

To understand potential connections between anion rotations and cation migration, Figure 5.7 shows displacement plots for the migration event in HT NSO occurring during a time window spanning 28.9-38.9 ps in the aiMD simulation performed at 850 K. This event involves the migration of two cations, "Na22" and "Na54." The displacement of each cation and the change in orientation of eight neighboring oxygen atoms (from two neighboring sulfate anions) about their central sulfur atoms is shown over a 10 ps window centered on the time when this migration evet occurs. In the plot, the black line represents the cation displacement vs. time;
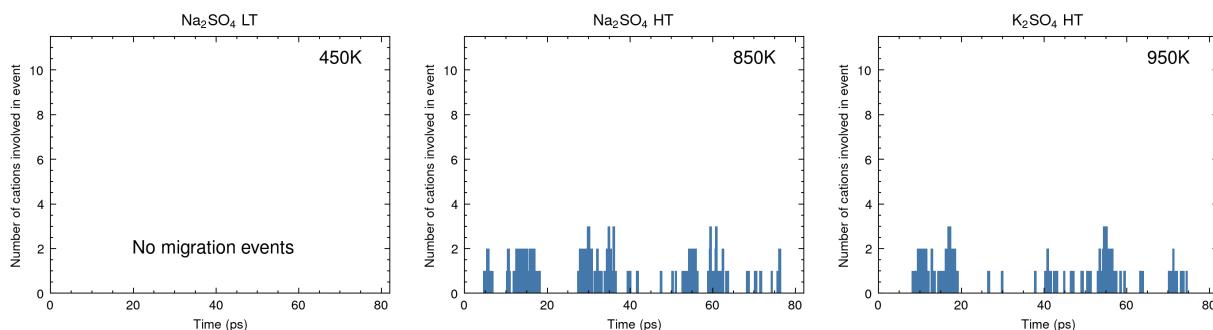
Figure 5.6 Migration events in LT NSO and HT NSO and KSO.

during this event, both Na22 and Na54 have a displacement of about 3Å, which is close to the

Na-Na nearest-neighbor distance of 3.4 Å. The blue lines represent orientation changes of the

oxygen atoms bonded to the two sulfur atoms identified in each plot's legend. There are 8 blue

lines; these correspond to the angular changes of the 8 S-O bond vectors from 2 nearest-neighbor

SO_4 anions. Correlation between the translational motion of Na54 and the reorientation of

tetrahedra "S3" clearly exists (right panel). Here, Na-ion migration begins around 4 ps, with the

reorientation of the S3 tetrahedra beginning soon afterwards. The migration and rotation exhibit

similar shapes, with rapid changes in Na-ion position and anion orientation occurring between 5

and 7 ps. The migration process ends at around 7 ps, at which point the cation and anion settle

into new basins on their respective potential energy surfaces. During this event the anion S3 has

rotated more than 120 degrees. Although the migration of Na22 happens at approximately the

same time (left panel of Figure 5.7), and thus appears to be moving in concert with Na54 (Figure

5.8), there is less evidence for correlation with anion reorientations in this case.

In total, these data show that even though the ionic conductivity of HT NSO is low, the

conductivity is not zero. When (infrequent) hopping events occur, the present calculations

provide evidence that some of these events exhibit correlations between cation migration and
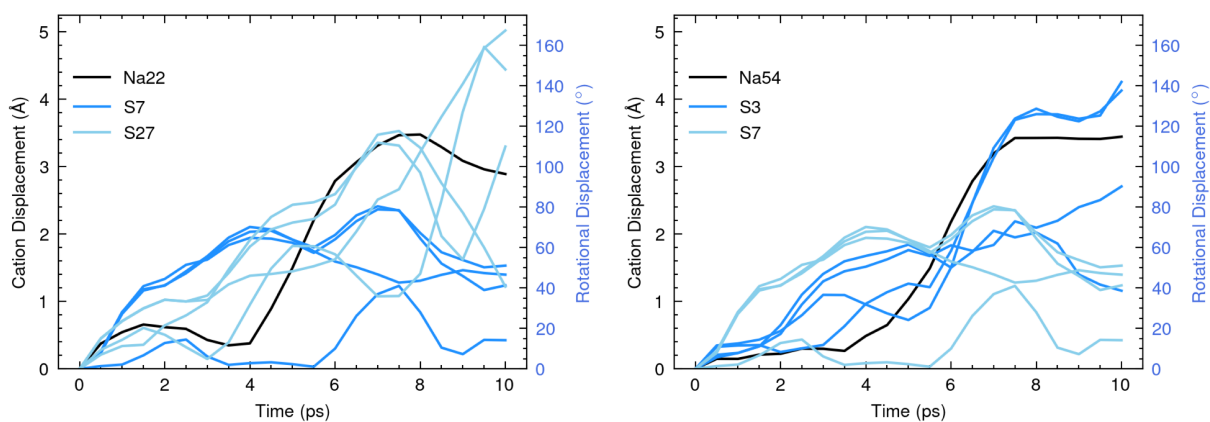
Figure 5.7 Displacement plots for migration event at 28.9ps in HT NSO.

anion rotations, similar to what was observed in HT LSO.

Figure 5.8 shows the real-space trajectory for the same event discussed above involving Na22 and Na54 and their neighboring sulfate anions (identified by sulfate index number). The migration of Na22 and Na54 are coordinated, as Na22 first migrates to a neighboring vacant site, after which Na54 migrates to fill the vacancy left behind by Na22. Concerted hoping of this nature is typical for ionic motion in solids having a high density of the mobile species.[20,88,105] The neighboring sulfate tetrahedra also rotate during this time; their position at the end of the event is superimposed over their initial, translucent position at the outset of the event.

Figure 5.9 shows displacement plots for KSO (simulated at 950 K) for a migration event that occurs during 10.5-20.5 ps. Here too, there appears to be correlation between cation motion and the reorientations of neighboring sulfate anions. During this event two K-ions, K23 and K51, each migrate approximately 4 Å, while anion S24 rotates more than 120 degrees. The real-space trajectories (not shown) also confirm the rotation of the SO_4^{2-} and the coordination between migrating cations.

Thus far we have examined correlations in space, time, and energetics. One may also expect that correlations exist in the vibrational properties of the anions and cations. Figure 5.10 plots the calculated power spectra for all the sulfates examined in this dissertation. (The power spectrum may be interpreted as a vibrational density of

Figure 5.8 Trajectory plot of migration event in HT NSO at 28.9ps. The Na ions move from B to E in the 10 ps event window, and the anions reorientation from the translucent positions to the opaque.

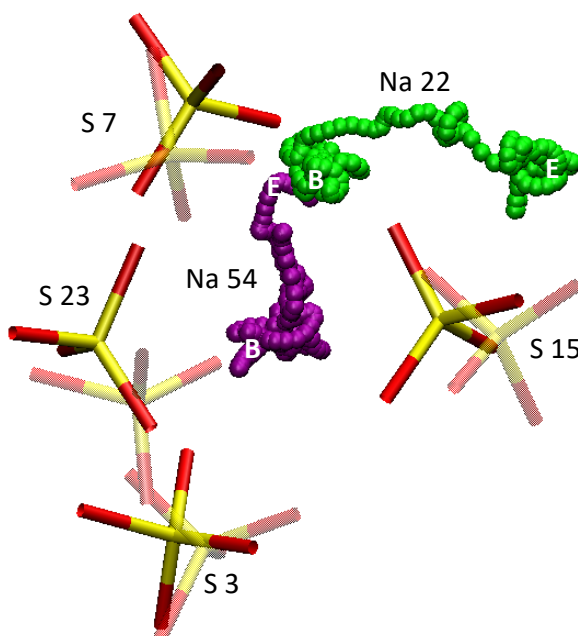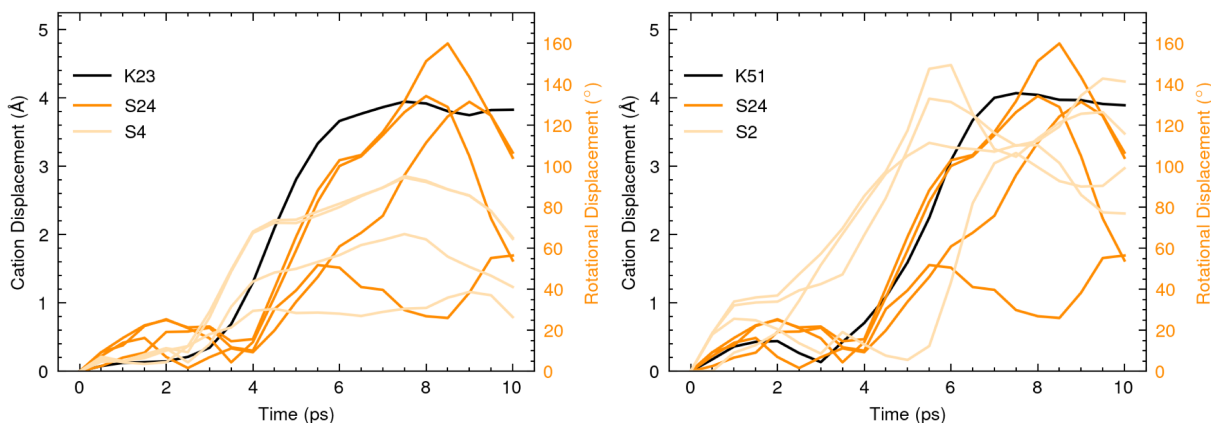Figure 5.9 Displacement plot for migration event in HT KSO. The black line represents the cation translation during the event time and the orange lines are the rotational displacement of the two nearest neighbor anions.

states which has been filtered to include cation translational motion and librational motion of the anions; translational motion of the anions has been filtered out.) Overlap in the spectrum of the anions and cations suggests the possibility for "resonance" or the transfer of momentum between these entities.

Figure 5.10 shows that the libration spectrum of SO_4^{2-} is similar in all of the sulfate systems, suggesting that SO_4^{2-}'s exhibit similar dynamics regardless of the cation composition. In contrast, the spectra associated with the cations exhibit more variation. For example, the Li^+ power spectrum is much broader than for either that of Na^+ or K^+. The Li+ spectrum covers a wider range of frequencies and overlaps with the middle-frequency mode of the SO_4^{2-} while the Na and K spectra only overlap with the lower mode. The similarity in the power spectra of K- and Na- sulfates mirrors their similar ionic conductivity. The unique vibrational behavior of Li-ions in Li_2SO_4 is also consistent with its uniquely high ionic conductivity.

5.4 Discussion

In the existing literature, low-conductivity NSO is often held as the foil of highly-conductive LSO: the low conductivity of the former is commonly blamed on its purported

absence of sulfate anion reorientations. Contrary to this common wisdom, the present work

shows clear evidence for dynamic anion disorder and paddlewheel-like behavior in both HT

NSO and HT KSO (at least when artificial vacancies are present in the lattice). The anion

reorientations exhibit a time scale on the same order (pico-seconds) as those of HT LSO.

Furthermore, the activation energy for reorientations in NSO is smaller than that in LSO.

However, in both HT KSO and NSO the rates of Na- and K-ion migration are slow, and neither

material comes close to matching the mobility observed for Li-ions in LSO.

     Our data suggests that the presence of anion rotations alone are not sufficient to ensure a

high ionic conductivity. It is well-known that ionic motion in solids is mediated by point defects

such as vacancies and interstitials, or by microstructural defects such as grain boundaries or
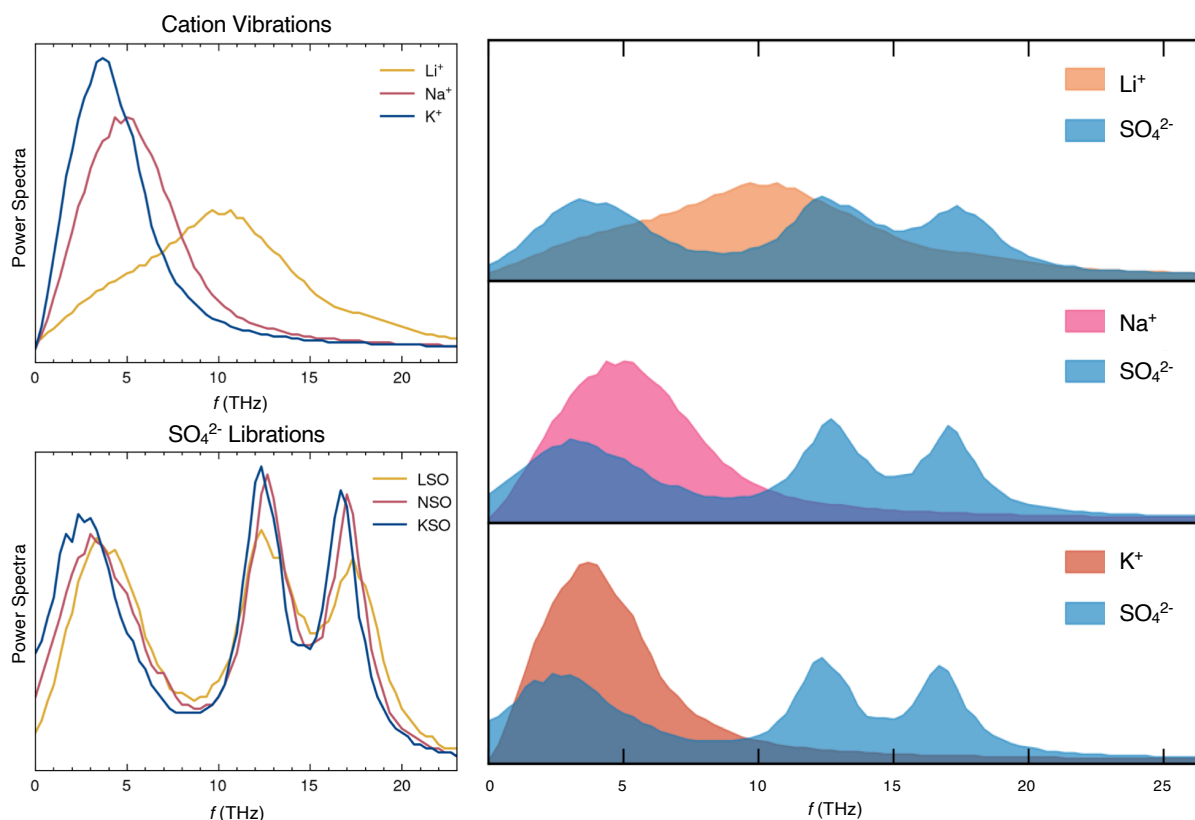
Figure 5.10 Vibrational power spectra data for cations and anions in HT LSO, NSO, and KSO.

dislocations.[106] In the FCC high temperature polymorph of LSO, Li can sit on two types of crystallographic sites, tetrahedral or octahedral. Structural studies have found that Li ions prefer to sit on the tetrahedral sites and the octahedral are left unoccupied.[17] These sites can act as "native vacancies," providing migration pathways through the material. DFT calculations on a 28 atom model revealed an energy difference of 3 meV/atom between a Li occupying a tetrahedral or octahedral site; it may be that the energetic preference is entropy based, but our calculations further suggests both sites are accessible to Li+ migrations. This is confirmed in the aiMD trajectories, where Li+ were observed moving through octahedral sites. Unlike HT LSO, HT NSO and KSO do not exhibit easily-accessible vacant cation sites in their hexagonal crystal structures. In sum, we hypothesize that the low conductivity in HT NSO and KSO results from the lack of a sufficient defect concentration, such as vacant cation sites. In short, migrating K and Na-ions have "no place to go" in these materials.

Figure 5.11 Ionic conductivity of NSO vs temperature for 0-23 mol% Y^{3+} dopants. Adapted from Ref 107.

Two observations support this hypothesis. First, when vacancies are inserted into the computational models of HT KSO and NSO, our simulations observe that migration events mediated by these vacancies can occur. As was shown above, these events exhibit correlations
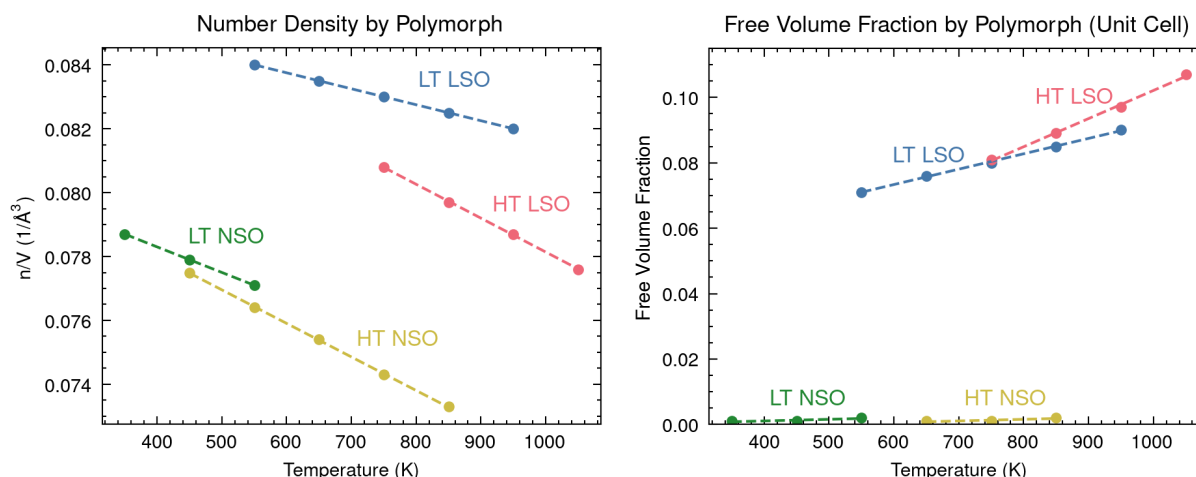
Figure 5.12 Free volume fraction and atomic number density of LSO and NSO polymorphs.

with anion reorientations similar to those seen in HT LSO. Secondly, experimental studies involving aliovalent doping of HT NSO have found that introducing dopants such as Y^{3+} can increase the conductivity by a factor of 100, as seen in Figure 5.11.[107] The addition of each Y^{3+} dopant into NSO substitutes for a single Na^{1+} ion and, to maintain charge neutrality, creates an additional two vacancies on the Na-ion sublattice. The amount of doping that is beneficial typically has an upper limit, however, as high doping levels can alter the crystal structure and/or result in the formation of new phases. In the case of Y^{3+}, the highest Na-ion conductivity occurred with 7.4 mol% dopant, and adding further Y began to reduce the conductivity. Based on these data, we conclude that a paddlewheel effect could be present in HT KSO and NSO if a sufficiently high concentration of vacancies are present in their crystal structures.

Unfortunately, screening for ionic conductors that could exhibit a paddlewheel effect is non-trivial. One strategy to conduct such a search could exploit the observation that anion rotation often 'turns on' in high-temperature polymorphs that exhibit expanded volumes (equivalently, lower densities) compared to the LT phase(s). This 'volume effect' played a prominent role in early debates about the paddlewheel effect.[90,108] Based on this, one could

57

screen materials based on their atomic number density (number of atoms/volume) or *free volume fraction* (FVF). The free volume fraction is related to the ratio of volume in the unit cell that is not occupied by atomic spheres and the cell volume. Specifically,

$$FVF = 1 - \frac{uncovered\ atomic\ sphere\ volume}{unit\ cell\ volume}.$$

Both volume-based measures for polymorphs of NSO and LSO are shown in Figure 5.12. The atomic number density and free volume fraction are near zero for both phases of NSO in the temperature range we studied. The values for HT NSO are slightly higher than that of LT NSO, which is consistent with the volume expansion inherent in the phase change. However, LT LSO still has higher values of n/V and FVF than HT NSO. It appears that these measures of free space in the structure are not completely sufficient descriptors to determine if rotations are present (HT NSO has rotations and LT LSO does not) or identify ionically conductive materials that benefit from anion rotations (HT NSO is a better conductor than LT LSO).

While the high temperature sulfates discussed here exist at too high a temperature to be SE materials, the paddlewheel effect can be found in room temperature materials.[37,88,109] To assist in the search for novel paddlewheel materials, a thorough understanding of the dynamics of simple benchmark systems is needed. NSO and KSO do display the hallmark anion reorientations and correlated cation displacements indicative of the paddlewheel effect but are not fast-ion conductors. This appears to be due to a lack of cation vacancies or defects in the cation sublattice to mediate the migration. This is an important addition to our understanding of these materials and the paddlewheel effect in general.

Chapter 6 Conclusions

From maximizing the capabilities of current technologies to finding new battery chemistries, improving our understanding of electrochemical processes will have many benefits. By employing first principles calculations on both practical and model systems, this project has sought to elucidate fundamental processes involving liquid and solid electrolytes for state-of-the art and emerging energy storage chemistries.

In Chapter 3, the adsorption and decomposition of EC on $LiCoO_2$ was explored with first principles calculations. There it was determined that surface Co ion on the low energy (10-14) surface adopt an intermediate spin state with an antiferromagnetic organization. The magnetic ordering of the surface Co impacted the adsorption geometries qualitatively and quantitatively, by stabilizing the surface Co and making EC coordination with surface Li the more energetically favorable adsorption geometry. This geometry is notable, as the coordination with Li could result in blocking a Li intercalation pathway into/out of the cathode and negatively impact the battery's capacity. Two exothermic decomposition products were predicted, and the kinetics of the more thermodynamically favorable reaction pathway was analyzed with the Nudged Elastic Band Method. The reaction was found to be kinetically limited with a high activation energy of 2.1eV. This implies that this reaction is unlikely to occur when the cathode is fully lithiated and under normal operating conductions (not in a state of overheating or overcharging).

Future studies in this system should explore surface-mediated electrolyte decomposition reactions when the cathode is in the (partially) charged state (i.e., when the Li content of the

cathode is decreased). Other studies have found that reducing the Li content changes the reactivity of the surface.[50] When the battery is fully charged (and the cathode is in its maximally-delithiated state), the lithium content of the cathode decreases by 50%, to $Li_{0.5}CoO_2$. In this state-of-charge, half the Co ions increase their oxidation state from +3 to a +4. This also changes the magnetic moment of the Co ions on the cathode surface, and potentially inside the bulk region of the cathode as well. Further studies may also wish to probe the impact of solvation on the decomposition dynamics. Our study modeled a single molecule on the (10-14) surface and employed the enthalphy of vaporization of EC to approximate the energetics of a liquid. Implicit and/or explicit solvation techniques[47,51] may allow for additional realism in modeling the surface and alter the reaction dynamics.

In Chapter 4, Li-ion migration in the high and low temperature polymorphs of Li_2SO_4 was simulated with aiMD. These simulations indicated that the paddlewheel effect is active in the high temperature phase, with Li+ migration activation energies of 0.48eV and anion reorientation activation energies of 0.4 eV. The aforementioned energetics, the anion reorientation auto-correlation function, and the presence of Li-ion migration events that correlate in space and in time with reorientations of the sulfate anions all indicate the presence of the paddlewheel effect.

It would be helpful in future studies to more carefully characterize the impact of the anion reorientation on the cation migration. This may be done in a coarse fashion by simulating the system with the anions positions frozen. Earlier work has shown that this constraint increases the energy for cation migration and reduces ionic conductivity.[37] A more elegant approach would be to simulate the system while constraining anion rotations, but allowing non-rotational

vibrations. Another approach would be to use a transition finding tool like the NEB to explore the migration barriers with and without rotations.

Another aspect of interest is the impact of guest cations in HT LSO. This material is noted for being a good conductor of not just Li+ ions, but a wide variety of iso- and aliovalent dopants. It is as of yet unknown if the paddlewheel mechanism extends to such dopants. Finally, one of the arguments used to argue against the importance of the paddlewheel effect in LSO are experiments on the ionic conductivity when LSO is doped with WO_4.[26] The tungstate ion is heavier than SO_4 and therefore has a greater moment of inertia and is not expected to reorient as readily. However, the presence of tungstate does not appear to hinder Li+ migration, leading Secco[26] and others to claim that the paddlewheel mechanism cannot be driving its high conductivity. There do not appear to be any computational studies on tungstate-doped LSO; simulating its dynamics may further our understanding of the underlying mechanisms.

NSO and KSO were the primary materials discussed in Chapter 5, and were introduced to draw comparisons with the behavior of LSO. The presence of a dynamic disorder in the high temperature polymorphs of both NSO and KSO is supported by the present aiMD simulations. Indeed, the anion reorientations in these compounds are comparable to those observed in LSO. Moreover, in cases where vacancies are inserted into the cation sublattice, evidence exists for correlated motion between anion rotations and cation migrations in both NSO and KSO. However, these materials remain poor ionic conductors.

Further work could be done to simulate the impact of aliovalent doping and resulting cation vacancies on the ionic conduction mechanism in NSO and KSO. Before beginning our simulation, one neutral cation was removed from each supercell to help mediate cation migrations. Further neutral cations could be removed, or replaced with aliovalent dopants. Other

interesting materials are $LiNaSO_4$ and $LiKSO_4$, both of which are ionically-conductive sulfates. Further work could be done to determine if the paddlewheel mechanism is active in these systems and if there are vacant sites that allow the cations to migrate.

The paddlewheel effect is a novel migration mechanism tied to high conductivity SE materials with dynamic disorder. These materials require sufficient free space for the anion to rotate as well as vacancies or defects to mediate cation migration. A high free volume fraction is one indicator that can point to a potential material for paddlewheel migrations, but must be coupled with vacancies in the cation sublattice for the paddlewheel mechanism to be effective.

Bibliography

1. Goodenough, J. B. & Kim, Y. Challenges for rechargeable Li batteries. *Chem. Mater.* **22**, 587–603 (2010).
2. Aurbach, D. *et al.* Review on electrode-electrolyte solution interactions, related to cathode materials for Li-ion batteries. *J. Power Sources* **165**, 491–499 (2007).
3. Kumar, N. & Siegel, D. J. Interface-Induced Renormalization of Electrolyte Energy Levels in Magnesium Batteries. *J. Phys. Chem. Lett* **7**, 874–881 (2016).
4. Xu, K. Electrolytes and Interphases in Li-Ion Batteries and Beyond. *Chem. Rev.* **114**, 11503–11618 (2014).
5. Xu, K. Nonaqueous liquid electrolytes for lithium-based rechargeable batteries. *Chem. Rev.* **104**, 4303–4417 (2004).
6. Minato, T. & Abe, T. Surface and interface sciences of Li-ion batteries: -Research progress in electrode–electrolyte interface-. *Prog. Surf. Sci.* **92**, 240–280 (2017).
7. Onuki, M. *et al.* Identification of the Source of Evolved Gas in Li-Ion Batteries Using 13C-labeled Solvents. *J. Electrochem. Soc.* **155**, A794 (2008).
8. Berkes, B. B., Schiele, A., Sommer, H., Brezesinski, T. & Janek, J. On the gassing behavior of lithium-ion batteries with NCM523 cathodes. *J. Solid State Electrochem.* **20**, 2961–2967 (2016).
9. Browning, K. L., Baggetto, L., Unocic, R. R., Dudney, N. J. & Veith, G. M. Gas evolution from cathode materials: A pathway to solvent decomposition concomitant to SEI formation. *J. Power Sources* **239**, 341–346 (2013).
10. Wuersig, A., Scheifele, W. & Novák, P. CO2 Gas Evolution on Cathode Materials for Lithium-Ion Batteries. *J. Electrochem. Soc.* **154**, A449 (2007).
11. Roth, E. P. & Orendorff, C. J. How electrolytes influence battery safety. *Electrochem. Soc. Interface* **21**, 45–49 (2012).
12. Roth, E. P. Abuse Response of 18650 Li-Ion Cells with Different Cathodes Using EC:EMC/LiPF6 and EC:PC:DMC/LiPF6 Electrolytes. *ECS Trans.* **11**, 19–41 (2008).
13. Kim, K. J., Balaish, M., Wadaguchi, M., Kong, L. & Rupp, J. L. M. Solid-State Li–Metal Batteries: Challenges and Horizons of Oxide and Sulfide Solid Electrolytes and Their Interfaces. *Advanced Energy Materials* vol. 11 2002689 (2021).
14. Benrath, A. & Drekopf, K. Über die elektrische Leitfähigkeit von Salzen und Salzgemischen. *Zeitschrift für Phys. Chemie* **99**, 57–70 (1921).
15. Lundén, A. Evidence for and against the paddle-wheel mechanism of ion transport in superionic sulphate phases. *Solid State Commun.* **65**, 1237–1240 (1988).
16. Rama Rao, S., Bheema Lingam, C., Rajesh, D., Vijayalakshmi, R. P. & Sunandana, C. S. Structural, conductivity and dielectric properties of Li2SO4. *Eur. Phys. J. Appl. Phys* **66**, 30906 (2014).
17. Nilsson, L., Thomas, J. O. & Tofield, B. C. The structure of the high-temperature solid

electrolyte lithium sulphate at 908K. *J. Phys. C Solid State Phys.* **13**, 6441–6451 (1980).

18.   Kvist, A. & Bengtzelius, A. Tracer diffusion and electrical conductivity of cubic lithium sulphate and a transport model for cubic sulphates. in *Fast Ion Transport in Solids* (ed. van Gool, W.) 193–9 (Noth-Holland Publishing Company, 1973).

19.   Tärneberg, R. & Lunden, A. Ion diffusion in the high-temperature phases Li2SO4, LiNaSO4, LiAgSO4 and Li4Zn(SO4)3. *Solid State Ionics* **90**, 209–220 (1996).

20.   Kaber, R., Nilsson, L., Andersen, N. H., Lunden, A. & Thomas, J. O. A single-crystal neutron diffraction study of the structure of the high-temperature rotor phase of lithium sulphate. *J. Phys. Condens. Matter* **4**, 1925–1933 (1992).

21.   Aronsson, R. *et al.* Solid sulphate electrolytes: the first examples of a strange ion transport mechanism. in *Radiation effects* vol. 75 79–84 (Taylor & Francis Group, 1983).

22.   Boerjesson, L. & Torell, L. M. Contrasting behavior of the SO42- symmetric Raman mode in high and low conducting sulfates. in *Proceedings - The Electrochemical Society* vols 86–1 21–28 (1986).

23.   Tärneberg, R. & Mellander, B. E. Ion transport in high temperature rotator phase solid electrolytes. *Solid State Ionics* **98**, 175–183 (1997).

24.   Wilmer, D., Feldmann, H. & Lechner, R. E. Cation and anion dynamics in the fast-ion conducting rotor phase of 7Li2SO4. *Phys. B Condens. Matter* **276–278**, 232–233 (2000).

25.   Natarajan, M. & Secco, E. A. Electrical Conductivity and Phase Transformation Studies on Pure and Doped (Mg 2+ , Zn 2+ , Cu 2+ , and Mn 2+) Crystals of K 2 SO 4. *Can. J. Chem.* **53**, 1542–1547 (1975).

26.   Secco, E. A. Paddle wheel mechanism in lithium sulfates: Arguments in defense and evidence against. *J. Solid State Chem.* **96**, 366–375 (1992).

27.   Gundusharma, U. M., MacLean, C. & Secco, E. A. Rotating sulfate ion contribution to electrical conductivity in Li2SO4 and LiNaSO4? *Solid State Commun.* **57**, 479–481 (1986).

28.   Satheesan Babu, C. & Tembe, B. L. Dynamics in superionic lithium sulphate lattice: paddle wheel versus percolation mechanism. *Chem. Phys. Lett.* **194**, 351–354 (1992).

29.   Eysel, W., Höfer, H. H., Keester, K. L. & Hahn, T. Crystal chemistry and structure of Na2SO4(I) and its solid solutions. *Acta Crystallogr. Sect. B* **41**, 5–11 (1985).

30.   Impey, R. W., Klein, M. L. & McDonald, I. R. Structural and dynamic properties of lithium sulphate in its solid electrolyte form. *J. Chem. Phys.* **82**, 4690–4698 (1985).

31.   Impey, R. W., Klein, M. L. & McDonald, I. R. Structure of the fast-ion conducting phase of soil lithium sulphate. *J. Phys. C Solid State Phys.* **17**, 3941–3944 (1984).

32.   Ferrario, M., Klein, M. L. & McDonald, I. R. Cation transport in lithium sulphate based crystals. *Mol. Phys.* **86**, 923–938 (1995).

33.   Sholl, D. S. & Steckel, J. A. *Density Functional Theory: A Practical Introduction*. *Density Functional Theory: A Practical Introduction* (John Wiley and Sons, 2009). doi:10.1002/9780470447710.

34.   Hohenberg, P. & Kohn, W. Inhomogeneous electron gas. *Phys. Rev.* **136**, B864 (1964).

35.   Kohn, W. & Sham, L. J. Self-consistent equations including exchange and correlation effects. *Phys. Rev.* **140**, (1965).

36.   Dudarev, S., Botton, G., Savrasov, S. Y., Humphreys, C. J. & Sutton, A. P. Electron-energy-loss spectra and the structural stability of nickel oxide: An LSDA+U study. *Phys. Rev. B - Condens. Matter Mater. Phys.* **57**, 1505–1509 (1998).

37.   Smith, J. G. & Siegel, D. J. Low-temperature paddlewheel effect in glassy solid

electrolytes. *Nat. Commun.* **11**, 1–11 (2020).

38. Keys, A. S., Hedges, L. O., Garrahan, J. P., Glotzer, S. C. & Chandler, D. Excitations Are Localized and Relaxation Is Hierarchical in Glass-Forming Liquids. *Phys. Rev. X* **1**, 1–15 (2011).

39. Burbano, M., Carlier, D., Boucher, F., Morgan, B. J. & Salanne, M. Sparse Cyclic Excitations Explain the Low Ionic Conductivity of Stoichiometric Li7La3Zr2 O12. *Phys. Rev. Lett.* **116**, 135901 (2016).

40. Ceder, G., Hautier, G., Jain, A. & Ong, S. P. Recharging lithium battery research with first-principles methods. *MRS Bull.* **36**, 185–191 (2011).

41. Mendoza-Hernandez, O. S., Ishikawa, H., Nishikawa, Y., Maruyama, Y. & Umeda, M. Cathode material comparison of thermal runaway behavior of Li-ion cells at different state of charges including over charge. *J. Power Sources* **280**, 499–504 (2015).

42. Kramer, D. & Ceder, G. Tailoring the Morphology of LiCoO2 : A First Principles Study. *Chem. Mater.* **21**, 3799–3809 (2009).

43. Qian, D. *et al.* Electronic Spin Transition in Nanosize Stoichiometric Lithium Cobalt Oxide. *J. Am. Chem. Soc.* **134**, 6096–6099 (2012).

44. Hong, L. *et al.* Electronic Structure of LiCoO 2 Surfaces and Effect of Al Substitution. *J. Phys. Chem. C* **123**, 8851–8858 (2019).

45. Han, B. *et al.* Role of LiCoO2 surface terminations in oxygen reduction and evolution kinetics. *J. Phys. Chem. Lett.* **6**, 1357–1362 (2015).

46. Gauthier, M. *et al.* Probing surface chemistry changes using LiCoO2-only electrodes in Li-ion batteries. *J. Electrochem. Soc.* **165**, A1377 (2018).

47. Tebbe, J. L., Fuerst, T. F. & Musgrave, C. B. Degradation of Ethylene Carbonate Electrolytes of Lithium Ion Batteries via Ring Opening Activated by LiCoO 2 Cathode Surfaces and Electrolyte Species. *ACS Appl. Mater. Interfaces* **8**, 26664–26674 (2016).

48. Giordano, L. *et al.* Chemical Reactivity Descriptor for the Oxide-Electrolyte Interface in Li-Ion Batteries. *J. Phys. Chem. Lett.* **8**, 3881–3887 (2017).

49. Tamura, T., Kohyama, M. & Ogata, S. Combination of first-principles molecular dynamics and XANES simulations for LiCoO 2 -electrolyte interfacial reactions in a lithium-ion battery. *Phys. Rev. B* **96**, 035107 (2017).

50. Kumar, N., Leung, K. & Siegel, D. J. Crystal Surface and State of Charge Dependencies of Electrolyte Decomposition on LiMn 2 O 4 Cathode. *J. Electrochem. Soc.* **161**, E3059–E3065 (2014).

51. Kumar, N., Radin, M. D., Wood, B. C., Ogitsu, T. & Siegel, D. J. Surface-mediated solvent decomposition in Li-Air batteries: Impact of peroxide and superoxide surface terminations. *J. Phys. Chem. C* **119**, 9050–9060 (2015).

52. Golubkov, A. W. *et al.* Thermal-runaway experiments on consumer Li-ion batteries with metal-oxide and olivin-type cathodes. *RSC Adv.* **4**, 3633–3642 (2014).

53. Jusys, Z., Binder, M., Schnaidt, J. & Behm, R. J. A novel DEMS approach for studying gas evolution at battery-type electrode|electrolyte interfaces: High-voltage LiNi0.5Mn1.5O4 cathode in ethylene and dimethyl carbonate electrolytes. *Electrochim. Acta* **314**, 188–201 (2019).

54. Okuno, Y., Ushirogata, K., Sodeyama, K., Shukri, G. & Tateyama, Y. Structures, Electronic States, and Reactions at Interfaces between LiNi0.5 Mn1.5O4 Cathode and Ethylene Carbonate Electrolyte: A First-Principles Study. *J. Phys. Chem. C* **123**, 2267–2277 (2019).

55. Kresse, G. & Hafner, J. Ab initio molecular-dynamics simulation of the liquid-metalamorphous- semiconductor transition in germanium. *Phys. Rev. B* **49**, 14251–14269 (1994).

56. Kresse, G. & Hafner, J. Ab initio molecular dynamics for liquid metals. *Phys. Rev. B - Condens. Matter Mater. Phys.* **47**, 558–561 (1993).

57. Kresse, G. & Furthmüller, J. Efficient iterative schemes for ab initio total-energy calculations using a plane-wave basis set. *Phys. Rev. B - Condens. Matter Mater. Phys.* **54**, 11169–11186 (1996).

58. Kresse, G. & Furthmüller, J. Efficiency of ab-initio total energy calculations for metals and semiconductors using a plane-wave basis set. *Comput. Mater. Sci.* **6**, 15–50 (1996).

59. Perdew, J. P., Burke, K. & Ernzerhof, M. Generalized gradient approximation made simple. *Phys. Rev. Lett.* **77**, 3865–3868 (1996).

60. G. Kresse & D. Joubert. From ultrasoft pseudopotentials to the projector augmented-wave method. *Phys. Rev. B - Condens. Matter Mater. Phys.* **59**, 1758–1775 (1999).

61. Blöchl, P. E. Projector augmented-wave method. *Phys. Rev. B* **50**, 17953–17979 (1994).

62. Jiří Klimeš, David R Bowler & Angelos Michaelides. Chemical accuracy for the van der Waals density functional. *J. Phys. Condens. Matter* **22**, 022201 (2010).

63. Lee, K., Murray, É. D., Kong, L., Lundqvist, B. I. & Langreth, D. C. Higher-accuracy van der Waals density functional. *Phys. Rev. B - Condens. Matter Mater. Phys.* **82**, 081101 (2010).

64. Klimeš, J., Bowler, D. R. & Michaelides, A. Van der Waals density functionals applied to solids. *Phys. Rev. B - Condens. Matter Mater. Phys.* **83**, 195131 (2011).

65. Dion, M., Rydberg, H., Schröder, E., Langreth, D. C. & Lundqvist, B. I. Van der Waals density functional for general geometries. *Phys. Rev. Lett.* **92**, 246401 (2004).

66. Román-Pérez, G. & Soler, J. M. Efficient implementation of a van der waals density functional: Application to double-wall carbon nanotubes. *Phys. Rev. Lett.* **103**, 096102 (2009).

67. Wang, L., Maxisch, T. & Ceder, G. Oxidation energies of transition metal oxides within the GGA+U framework. *Phys. Rev. B - Condens. Matter Mater. Phys.* **73**, 195107 (2006).

68. Maram, P. S., Costa, G. C. C. & Navrotsky, A. Experimental Confirmation of Low Surface Energy in LiCoO$_2$ and Implications for Lithium Battery Electrodes. *Angew. Chemie Int. Ed.* **52**, 12139–12142 (2013).

69. Sugiyama, J. *et al.* Frustrated magnetism in the two-dimensional triangular lattice of LixCoO2. *Phys. Rev. B* **72**, 144424 (2005).

70. Hong, C. S., Wakslak, R., Finston, H. & Fried, V. Some Thermodynamic Properties of Systems Containing Propylene Carbonate and Ethylene Carbonate. *J. Chem. Eng. Data* **27**, 146–148 (1982).

71. Rappé, A. K., Casewit, C. J., Colwell, K. S., Goddard, W. A. & Skiff, W. M. UFF, a Full Periodic Table Force Field for Molecular Mechanics and Molecular Dynamics Simulations. *J. Am. Chem. Soc.* **114**, 10024–10035 (1992).

72. Sanville, E., Kenny, S. D., Smith, R. & Henkelman, G. Improved Grid-Based Algorithm for Bader Charge Allocation. *J. Comput. Chem.* **28**, 899–908 (2007).

73. Tang, W., Sanville, E. & Henkelman, G. A grid-based Bader analysis algorithm without lattice bias. *J. Phys. Condens. Matter* **21**, 84204–84211 (2009).

74. Henkelman, G., Arnaldsson, A. & Jónsson, H. A fast and robust algorithm for Bader decomposition of charge density. *Comput. Mater. Sci.* **36**, 354–360 (2006).

75. Yu, M. & Trinkle, D. R. Accurate and efficient algorithm for Bader charge integration. *J. Chem. Phys.* **134**, 64111 (2011).

76. Henkelman, G. & Jónsson, H. Improved tangent estimate in the nudged elastic band method for finding minimum energy paths and saddle points. *J. Chem. Phys.* **113**, 9978–9985 (2000).

77. Henkelman, G., Uberuaga, B. P. & Jónsson, H. Climbing image nudged elastic band method for finding saddle points and minimum energy paths. *J. Chem. Phys.* **113**, 9901–9904 (2000).

78. Nord, A. G. Crystal structure of β-Li 2 SO 4. *Acta Crystallogr. Sect. B Struct. Crystallogr. Cryst. Chem.* **32**, 982–983 (1976).

79. Sun, J. *et al.* Accurate first-principles structures and energies of diversely bonded systems from an efficient density functional. *Nat. Chem.* **8**, 831–836 (2016).

80. Peng, H., Yang, Z. H., Perdew, J. P. & Sun, J. Versatile van der Waals density functional based on a meta-generalized gradient approximation. *Phys. Rev. X* **6**, 041005 (2016).

81. Aronsson, R. & Torell, L. M. Elastic constants of a solid-electrolyte fcc Li2SO4 single crystal obtained by Brillouin scattering. *Phys. Rev. B - Condens. Matter Mater. Phys.* **36**, 4926–4934 (1987).

82. Mellander, B. E. & Nilsson, L. Thermal Expansion of Lithium Sulphate. *Zeitschrift fur Naturforsch. - Sect. A J. Phys. Sci.* **38**, 1396–1399 (1983).

83. Swanson, H. E. & of Standards, U. S. N. B. Section 6. - Data for 60 substances. in *Standard X-ray Diffraction Powder Patterns* 97 (United States. Government Printing Office., 1968).

84. Birch, F. Finite elastic strain of cubic crystals. *Phys. Rev.* **71**, 809–824 (1947).

85. Lunden, A. Ionic Conduction in Sulphates. in *Fast Ion Transport in Solids* 181–201 (Springer Netherlands, 1993). doi:10.1007/978-94-011-1916-0_10.

86. Balaya, P. & Sunandana, C. S. Quenched lithium sulphate. *J. Phys. Chem. Solids* **55**, 39–48 (1994).

87. Suleiman, B. M., Gustavsson, M., Karawacki, E. & Lundén, A. Thermal properties of lithium sulphate. *J. Phys. D. Appl. Phys.* **30**, 2553–2560 (1997).

88. Zhang, Z. & Nazar, L. F. Exploiting the paddle-wheel mechanism for the design of fast ion conductors. *Nat. Rev. Mater.* **7**, 389–405 (2022).

89. Tanaka, K., Naruse, H., Morikawa, H. & Marumo, F. Phase-transition process of Na2SO4(III) to Na2SO4(I) and anharmonic thermal vibration. *Acta Crystallogr. Sect. B* **47**, 581–588 (1991).

90. Gomathy, S., Gopalan, P. & Kulkarni, A. R. Effect of homovalent anion doping on the conductivity and phase transitions in Na2SO4. *J. Solid State Chem.* **146**, 6–12 (1999).

91. Naruse, H., Tanaka, K., Morikawa, H., Marumo, F. & Mehrotra, B. N. Structure of Na2SO4(I) at 693 K. *Acta Crystallogr. Sect. B* **43**, 143–146 (1987).

92. Arnold, H., Kurtz, W., Richter-Zinnius, A., Bethke, J. & Heger, G. The phase transition of K2SO4 at about 850 K. *Acta Crystallogr.* **B37**, 1643–1651 (1981).

93. Kurtz, W. The Phase Transition of Potassium Sulfate. *Zeitschrift fur Naturforsch. - Sect. A J. Phys. Sci.* **47**, 1039–1046 (1992).

94. Miyake, M., Morikawa, H. & Iwai, S. Structure reinvestigation of the high-temperature form of K2SO4. *Acta Crystallogr. Sect. B Struct. Crystallogr. Cryst. Chem.* **36**, 532–536 (1980).

95. Bredig, M. A. Anion rotation in crystal lattices of A2BX4 compounds. *J. Phys. Chem.* **47**,

587–590 (1943).

96. Choi, B. K. & Lockwood, D. J. Raman spectrum of Na2SO4 (phases I and II). *Solid State Commun.* **76**, 863–866 (1990).

97. Brand, R., Lunkenheimer, P. & Loidl, A. Relaxation dynamics in plastic crystals. *J. Chem. Phys.* **116**, 10386–10401 (2002).

98. Yazhenskikh, E., Jantzen, T., Kobertz, D., Hack, K. & Müller, M. Critical thermodynamic evaluation of the binary sub-systems of the core sulphate system Na2SO4–K2SO4–MgSO4–CaSO4. *Calphad Comput. Coupling Phase Diagrams Thermochem.* **72**, 102234 (2021).

99. Börjesson, L. & Torell, L. M. Reorientational motion in superionic sulfates: A Raman linewidth study. *Phys. Rev. B* **32**, 2471–2477 (1985).

100. Börjesson, L. & Torell, L. M. Raman Scattering evidence of rotating SO42- in solid sulphate electrolytes. *Solid State Ionics* **18**–**19**, 582–586 (1986).

101. van den Berg, A. J. & Tuinstra, F. The space group and structure of α-K2SO4. *Acta Crystallogr. Sect. B Struct. Crystallogr. Cryst. Chem.* **34**, 3177–3181 (1978).

102. Choi, B. K. Ionic conductivity of Na2SO4 (I) crystals. *Solid State Ionics* **58**, 133–138 (1992).

103. Choi, B.-K. & Lockwood, D. J. Ionic conductivity and the phase transitions in Na2SO4. *Phys. Rev. B* **40**, 4683–4689 (1989).

104. Ahmad, M. M. Ionic conduction and dielectric relaxation in polycrystalline Na 2SO4. *Solid State Ionics* **177**, 21–28 (2006).

105. Wilmer, D., Feldmann, H., Lechner, R. E. & Combet, J. Sodium ion conduction in plastic phases: Dynamic coupling of cations and anions in the picosecond range. *J. Mater. Res.* **20**, 1973–1978 (2005).

106. Tilley, R. J. D. *Defects in Solids*. *Defects in Solids* (John Wiley and Sons, 2008). doi:10.1002/9780470380758.

107. Höfer, H. H., Eysel, W. & Alpen, U. v. Ionic conductivity of Na2SO4I solid solutions. *Mater. Res. Bull.* **13**, 265–270 (1978).

108. Hull, S. Superionics: crystal structures and conduction processes. *Reports Prog. Phys.* **67**, 1233 (2004).

109. Zhang, Z., Roy, P.-N., Li, H., Avdeev, M. & Nazar, L. F. Coupled Cation−Anion Dynamics Enhances Cation Mobility in Room-Temperature Superionic Solid-State Electrolytes. *J. Am. Chem. Soc* **141**, 19360–19372 (2019).